Physics of the Earth and Planetary Interiors 277 (2018) 10–29

Contents lists available at ScienceDirect

Physics of the Earth and Planetary Interiors

journal homepage: www.elsevier.com/locate/pepi

Linking lowermost mantle structure, core-mantle boundary heat flux and mantle plume formation

Mingming Li[a,*], Shijie Zhong[a], Peter Olson[b]

[a] Department of Physics, University of Colorado, Boulder, CO, USA
[b] Department of Earth and Planetary Sciences, University of New Mexico, Albuquerque, NM, USA

ARTICLE INFO

Keywords:
CMB heat flux
Mantle plume
Thermochemical piles
Large igneous provinces
Geomagnetic superchrons

ABSTRACT

The dynamics of Earth's lowermost mantle exert significant control on the formation of mantle plumes and the core-mantle boundary (CMB) heat flux. However, it is not clear if and how the variation of CMB heat flux and mantle plume activity are related. Here, we perform geodynamic model experiments that show how temporal variations in CMB heat flux and pulses of mantle plumes are related to morphologic changes of the thermochemical piles of large-scale compositional heterogeneities in Earth's lowermost mantle, represented by the large low shear velocity provinces (LLSVPs). We find good correlation between the morphologic changes of the thermochemical piles and the time variation of CMB heat flux. The morphology of the thermochemical piles is significantly altered during the initiation and ascent of strong mantle plumes, and the changes in pile morphology cause variations in the local and the total CMB heat flux. Our modeling results indicate that plume-induced episodic variations of CMB heat flux link geomagnetic superchrons to pulses of surface volcanism, although the relative timing of these two phenomena remains problematic. We also find that the density distribution in thermochemical piles is heterogeneous, and that the piles are denser on average than the surrounding mantle when both thermal and chemical effects are included.

1. Introduction

The solid Earth evolves as an integrated system, in which the various dynamical elements are coupled. In particular, the formation of mantle plumes, the variation of core-mantle boundary (CMB) heat flux and the changes of lowermost mantle structure significantly influence each other. Resolving the interplay between these elements is critical for a more comprehensive understanding of whole Earth dynamics.

It is widely accepted that mantle plumes develop from instability of thermal boundary layers, with the thermal boundary layer above the CMB being the most often assumed source. Typically, a mantle plume is thought to initiate with a big plume head (Whitehead and Luther, 1975; Olson and Nam, 1986). Large igneous provinces (LIPs), extremely large, rapid accumulations of volcanic crust are thought to result from plume heads impinging on the lithosphere from below (Richards et al., 1989; Campbell and Griffiths, 1992; Campbell, 2005). Some LIP events are found to coincide in time with episodic mass extinctions (Courtillot and Renne, 2003; Courtillot and Olson, 2007) and some LIPs have been implicated in the breakup of supercontinents (Courtillot et al., 1999; Ernst and Bleeker, 2010). Geochronology studies also show that there is correlation between clustered LIP events and peaks in the frequency of zircon ages (Condie et al., 2014, 2017). The episodic nature of the LIP emplacement implies that strong mantle plumes form episodically and have finite lifetimes, rather than being permanent dynamical structures. For example, the LIP population and the total volume of intraplate igneous rocks produced reached maxima during the mid-Cretaceous, with a rapid increase at around 125 Ma (Larson, 1991; Olson and Amit, 2015), which indicates an increase in the rate of plume formation during the mid-Cretaceous or earlier.

Mantle plume activity is supposed to be linked to the CMB heat flux (Davies, 1988; Zhong, 2006; Leng and Zhong, 2008). The episodic formation of mantle plumes as suggested by the LIP events indicates significant time variations in the CMB heat flux, which may alter the frequency of the geomagnetic polarity reversals (Olson et al., 2014). Throughout the lifetime of the Earth's geomagnetic field, the time duration of polarity chrons, that is, the time between geomagnetic polarity reversals, varies significantly (Cande and Kent, 1995). Geomagnetic superchrons (long time intervals without polarity reversals) repeat every ~150–200 Myrs during the Phanerozoic with each superchron lasting for about 40 Myrs. Between superchrons are still longer intervals characterized by frequent polarity reversals with reversal rates sometimes exceeding one reversal per 40 kyrs (Cande and

* Corresponding author.
E-mail address: Mingming.Li@colorado.edu (M. Li).

https://doi.org/10.1016/j.pepi.2018.01.010
Received 30 August 2017; Received in revised form 6 December 2017; Accepted 12 January 2018
Available online 16 January 2018
0031-9201/

Kent, 1995; Courtillot and Olson, 2007; Olson et al., 2014). Numerical dynamo simulations show that magnetic polarity reversals are significantly controlled by the CMB heat flux, with less frequent reversals when the CMB heat flux is low (Olson et al., 2014). This is because polarity reversal rates in numerical dynamos are sensitive to the vigor of outer core convection. When the vigor of outer core convection decreases (because the CMB heat flux is low) the time variability of the magnetic field in the core also decreases, resulting in less frequent reversals. The repetitive occurrence of geomagnetic superchrons during the Phanerozoic thus suggests that the CMB heat flux varies quasi-periodically during this time. Interestingly, the occurrence of the latest superchron (the Cretaceous Normal Polarity Superchron, or CNS) between ~120 and ~83 Ma is concurrent with the peaks of LIP events during this time (Olson and Amit, 2015), which again suggests that the formation of mantle plumes and variation of CMB heat flux are related. The real question is then: how are they related?

The CMB heat flux and the formation of mantle plumes are both significantly controlled by the structure and dynamics of Earth's lowermost mantle. Seismically prominent features in the lowermost mantle include the two large low shear velocity provinces (LLSVPs) beneath Africa and Pacific, which are surrounded by regions with higher than average seismic velocities (e.g., Li and Romanowicz, 1996; Masters et al., 2000; Gu et al., 2001; Grand, 2002; Dziewonski et al., 2010; Ritsema et al., 2011; Garnero et al., 2016). The two LLSVPs are not identical; they exhibit different lateral geometry, height and internal structure (Su et al., 1994; Ni and Helmberger, 2003; He and Wen, 2012; French and Romanowicz, 2015; Cottaar and Lekic, 2016). Their slope and height above the CMB are locally variable and are different for each LLSVP (e.g., Cottaar and Lekic, 2016). Seismic observations indicate that the LLSVPs are probably compositionally distinct with respect to the surrounding mantle (e.g., Masters et al., 2000; Wen et al., 2001; Ni et al., 2002; Trampert et al., 2004; He and Wen, 2012).

As suggested by geodynamic experiments, compositionally distinct and intrinsically denser materials can be pushed by convection into thermochemical piles that resemble the LLSVPs (McNamara and Zhong, 2005; Zhang et al., 2010; Bower et al., 2013; Zhong and Rudolph, 2015), with strong thermal plumes preferentially forming at the edges of the thermochemical piles (Tan et al., 2011; Li and Zhong, 2017). Like CMB heat flux and plume initiation, most numerical simulations show that the morphology of thermochemical piles also changes significantly with time (Zhang et al., 2010; Li et al., 2014a; Zhong and Rudolph, 2015). Laboratory experiments show a particular form of pile variability: for certain ranges of their intrinsic density anomaly, the thermochemical piles oscillate, alternating between phases of growth (that is, greater elevation and smaller lateral footprint on the CMB) and collapse (that is, less elevation and larger lateral footprint on the CMB) (Davaille, 1999; Le Bars and Davaille, 2004).

However, questions remain as to (1) how the changes of the morphology of thermochemical piles (e.g., LLSVPs), the variation of CMB heat flux and the episodic formation of mantle plumes are related, and (2) why mantle dynamics supports this style of time dependence? An answer to the first question is suggested by the inference that the thermochemical piles are hotter than their surroundings, and the CMB heat flux is dominated by the relatively cold regions outside of piles (Zhang and Zhong, 2011), so that the size of the footprint of the thermochemical piles controls the CMB heat flux. One possible scenario proposed by Olson and Amit (2015) is that, during the growth phase of thermochemical piles, their lateral footprints decrease, leading to an increase of CMB heat flux. Conversely, collapse of thermochemical piles increases their footprints, reduces the CMB heat flux, and at the same time, generates thermal plumes near the pile edges. It is thus interesting to test this hypothesis with self-consistent geodynamic models, to better understand what causes the growth and collapse of the intrinsically dense thermochemical piles, and how they are related to the formation of plumes and changes of CMB heat flux. In addition, these same geodynamic models offer the means to quantify how varying physical parameters of the lowermost mantle affect the correlation among changing morphology of thermochemical piles, formation of mantle plumes and variation of CMB heat flux.

In this study, we perform thermochemical convection calculations to study the interaction between mantle plumes and thermochemical piles in the lowermost mantle, and its effects on CMB heat flux. We focus on identifying the mechanism that leads to simultaneous formation of mantle plumes, variation of CMB heat flux and change of thermochemical pile morphology in the lowermost mantle.

2. Method

We model thermochemical convection in a 2D Cartesian box by numerically solving the following conservation equations of mass, momentum and energy under the Boussinesq approximation:

$$\nabla\cdot\vec{u} = 0, \tag{1}$$

$$-\nabla P + \nabla\cdot(\eta\,\dot{\epsilon}) = Ra(T-BC)\hat{z}, \tag{2}$$

$$\frac{\partial T}{\partial t} + (\vec{u}\cdot\nabla)T = \nabla\cdot(\nabla T) + H, \tag{3}$$

where $\vec{u}$ is the velocity, P is the dynamic pressure, η is the viscosity, $\dot{\epsilon}$ is the strain rate, Ra is the Rayleigh number, T is the temperature, B and C are the buoyancy number and the composition, respectively. The unit vector in the vertical direction is $\hat{z}$, t is the time, and H is the internal heating rate. The equations are non-dimensionalized through introduction of the following characteristic scales (primed variables are dimensionless):

$$\begin{aligned} x_i &= D_0 x_i', \\ u_i &= U_0 u_i', \\ T &= \Delta T T', \\ t &= t' D_0/U_0, \\ P &= \eta U_0/D_0 P', \\ U_0 &= \kappa_0/D_0, \end{aligned} \tag{4}$$

where D_0 and κ_0 are the thickness of the Earth's mantle and the reference diffusivity, respectively and ΔT is the reference temperature. The Rayleigh number is defined as:

$$Ra = \frac{\rho_0 g \alpha_0 \Delta T D_0^3}{\kappa_0 \eta_0}, \tag{5}$$

where ρ_0, α_0 and η_0 are the reference density (e.g., the density for the background mantle), reference thermal expansivity, and reference viscosity, respectively. Reference values are listed in Table 1. We use our modified 2D Citcom code (Moresi and Solomatov, 1995) that includes multiple compositional components to solve these equations.

All boundaries are free-slip. The top and bottom boundaries are isothermal with $T = 0$ and $T = 1$ (non-dimensional), respectively, and the side boundaries are insulating. The models are entirely basal heated, an approximation that yields realistic average mantle temperatures in 2D Cartesian geometry (O'Farrell and Lowman, 2010). The 2D box in our models has an aspect ratio of 3, and the computational domain is divided into 384 × 128 (horizontal × vertical) elements.

Table 1
Parameters used in this study.

Parameters	Reference value
Mantle thickness D_0	2890 km
Mantle density ρ_0	3300 kg/m^3
Thermal expansivity α_0	1×10^{-5} K^{-1}
Thermal diffusivity κ_0	1×10^{-6} m^2/s
Gravitational acceleration g	9.8 m/s^2
Temperature change across the mantle ΔT	3000 K
Reference viscosity η_0	2.3×10^{21}, 7.8×10^{20} Pa s

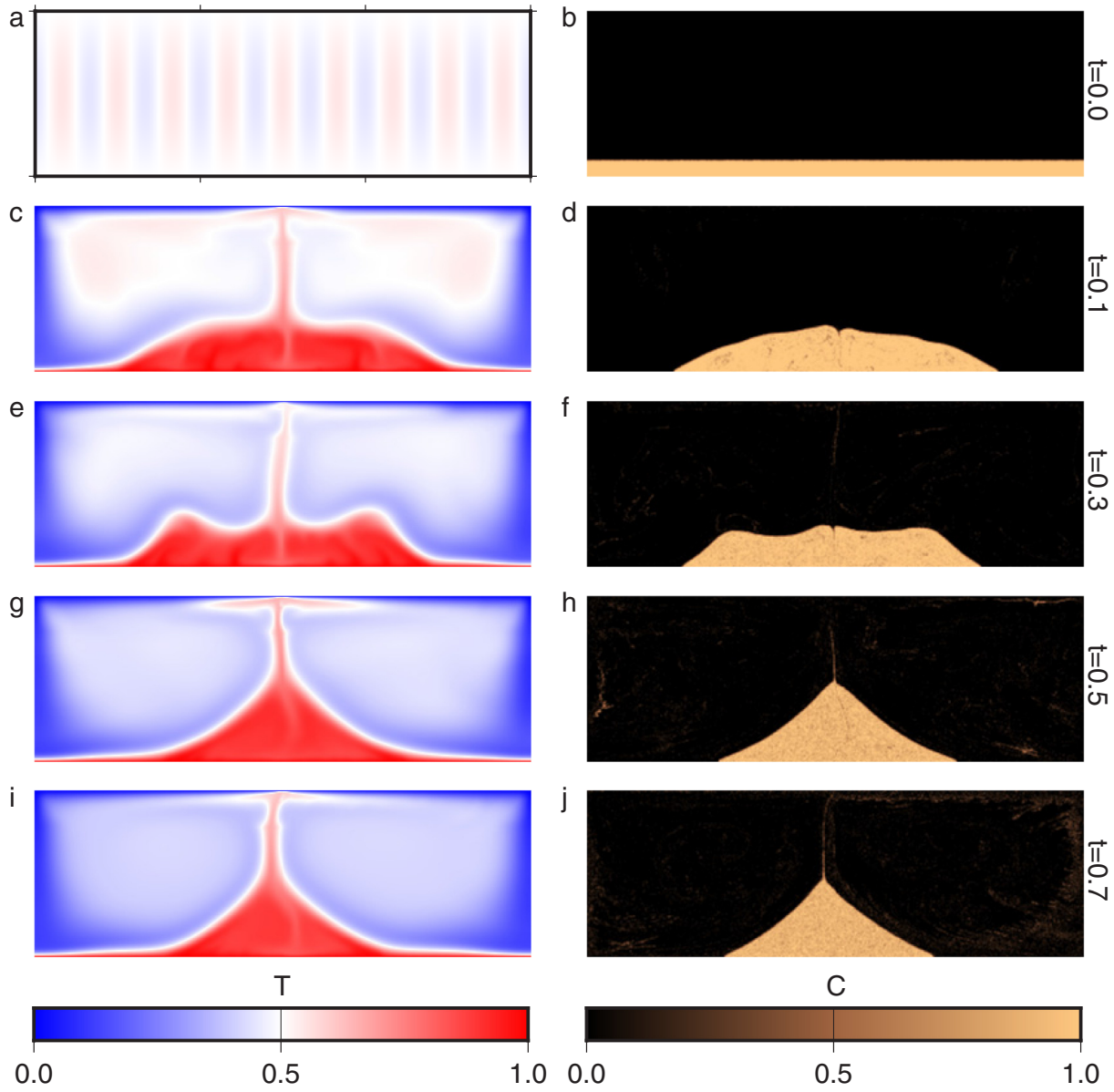

Fig. 1. Snapshots of temperature field (left) and the corresponding composition field (right) for case 1 at t = 0.0 (a, b), 0.1 (c, d), 0.3 (e, f), 0.5 (g, h), and 0.7 (i, j).

All models start with an initial temperature of $T = 0.5$ plus thermal perturbations (Fig. 1a). A layer of uniformly dense material initially occupies the lowermost 300 km for most cases (Fig. 1b). The intrinsically dense material is characterized by a buoyancy number $B = \Delta\rho/\rho_0\alpha_0\Delta T$, where $\Delta\rho$ is the compositional density anomaly between the intrinsically dense material and the background mantle.

It has been suggested that the phase transition from Perovskite (pv) to post-Perovskite (ppv) in the lowermost mantle can increase the CMB heat flux (Nakagawa and Tackley, 2011) and decrease the stability of thermochemical piles (Li et al., 2014b). We therefore explore the effects of the ppv phase in cases 5–8 (Table 2). The approach to model the phase transition is similar to previous studies (e.g., Christensen and Yuen, 1985; Zhong and Gurnis, 1994; Nakagawa and Tackley, 2005). The phase function is defined as:

$$\Gamma(\pi) = 0.5 + 0.5\tanh\left(\frac{\pi}{w}\right), \tag{6}$$

where π is the dimensionless excess pressure and w is the width of the phase transition. The excess pressure π is defined as:

Table 2
All cases used in this study.

Case	*Ra*	*B*	*h* (km)	η_{ppv}	T_{ppv}
1	1e7	0.6	300	N/A	N/A
2	1e7	0.8	300	N/A	N/A
3	1e7	0.6	150	N/A	N/A
4	3e7	0.6	300	N/A	N/A
5	1e7	0.6	300	1.0	0.473
6	1e7	0.6	300	0.01	0.473
7	1e7	0.6	300	0.01	0.39
8	1e7	0.6	300	0.001	0.39

Ra = Rayleigh number; *B* = Buoyancy number; *h* = initial thickness of the intrinsically dense layer; η_{ppv} = viscosity reduction of post-Perovskite; T_{ppv} = temperature for the ppv phase transition at depth of D_{ppv}.

$$\pi = D - D_{ppv} - \gamma(T - T_{ppv}), \tag{7}$$

where D is the depth, and $\gamma_{ppv} = 0.385$ is the Clapeyron slope, both dimensionless. Using values of the parameters in the Table 1, the dimensionalized Clapeyron slope (which is scaled by the term $\rho g D/\Delta T$) is

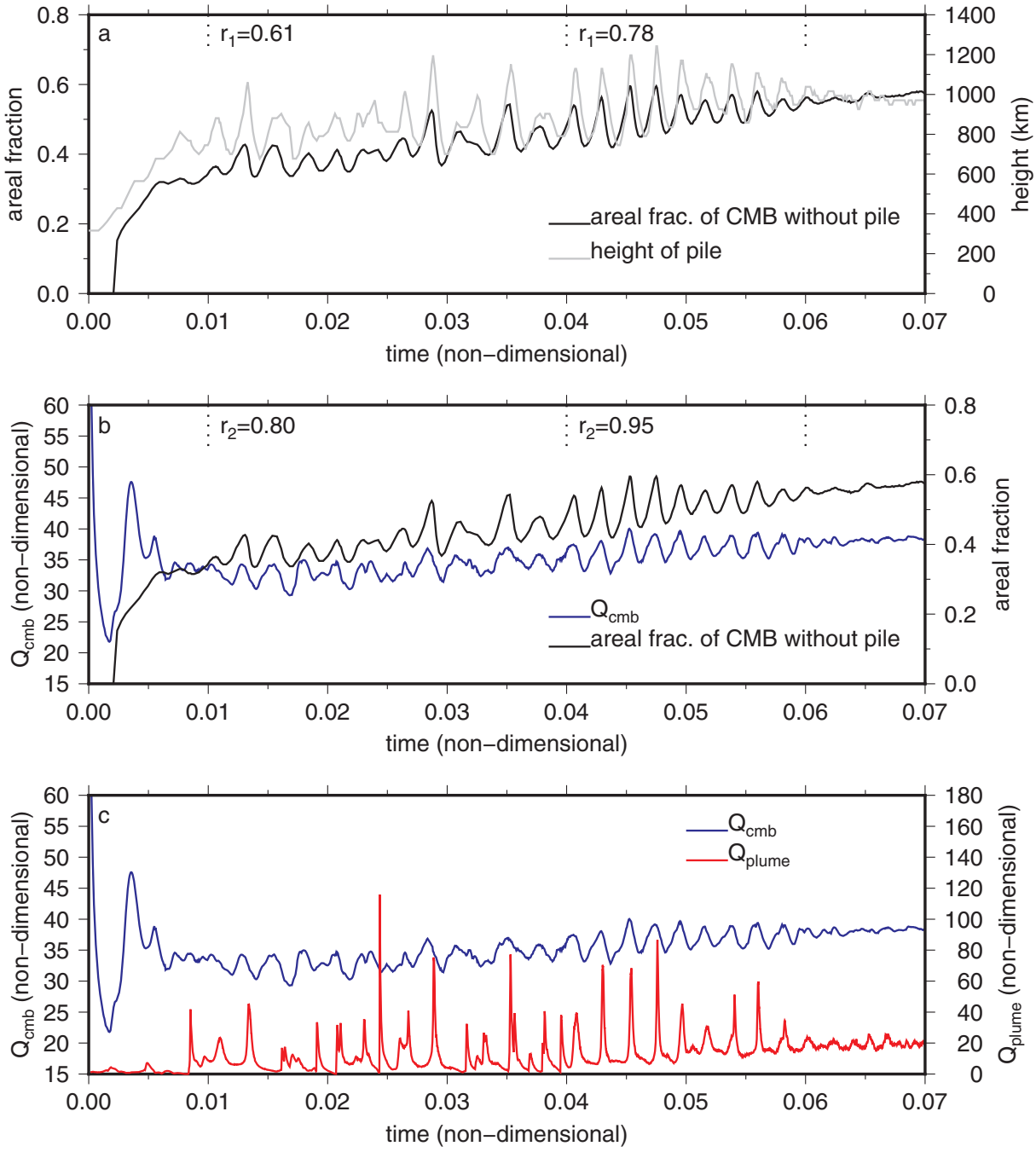

Fig. 2. Time evolution of height of thermochemical pile, areal fraction of the CMB without pile material, global CMB heat flux (Q_{cmb}), and plume heat flux at 300 km depth (Q_{plume}) for case 1. r_1 and r_2 are the correlation efficiencies for the correlations between the height of the pile and the areal fraction of CMB without pile material, and between the areal fraction of CMB without pile material and the CMB heat flux, respectively. We compute separate values for r_1 and r_2 during each time interval defined by the dotted short lines.

12 MPa/K. D_{ppv} is the depth for the phase transition at temperature T_{ppv}. We use D_{ppv} = 0.9343, which is dimensionalized to a depth of 2700 km. We use T_{ppv} = 0.473 or a dimensional temperature of 1420 K in cases 5 and 6. Note that this is the potential temperature since the adiabatic temperature increase with depth is removed in our models under the Boussinesq approximation. The adiabatic temperature at 2700 km depth is ~1218 K (e.g., calculated by increasing the temperature from the surface of 273 K to 2700 km depth with a temperature gradient of 0.35 K/km). Thus, T_{ppv} = 0.473 in our models additional to the adiabatic temperature increase at 2700 km depth is equivalent to a temperature of ~2640 K for the true Earth. In cases 7 and 8, we use T_{ppv} = 0.39, which is equivalent to a decrease of the threshold temperature for the phase transition, or alternatively, an increase of mantle temperature with the increase of the reference temperature and/or adiabatic temperature gradient. We assume a 1% density increase for the phase transition, and the width of the phase transition is 30 km. These parameters for the ppv phase transition are consistent with mineral physics results (e.g., Murakami et al., 2004) and are similar to that used in previous numerical modeling studies (Nakagawa and Tackley, 2011; Li et al., 2014b). We do not consider the effects of latent heating of this phase transition under the Boussinesq approximation, which were found to be small on the large-scale convection (Nakagawa and Tackley, 2004).

The viscosity is expressed as $\eta = \eta_0 \exp[\Gamma \ln(\eta_{ppv}) + A(0.5-T)]$,

where A is the activation coefficient. Below 100 km depth, we use $A = 9.21$, which results in 4 orders of viscosity change due to changes of temperature. To produce plate-like lithosphere, we use $A = 11.51$ for the uppermost 100 km, which leads to 5 orders of maximum changes in the near-surface viscosity. We introduce weak zones near the surface at the left and right side boundaries and in the middle of the model box (King et al., 1992). The width and depth of the weak zones are both 200 km, and the viscosity in the weak zones is reduced by 100 times compared to the rest of the surface. We employ a 30× viscosity increase across the 670-km depth from the upper mantle to lower mantle, by increasing η_0 from 1 to 30 (Hager, 1984). We also investigate the effects of weak ppv (Hunt et al., 2009; Ammann et al., 2010) in some models, by changing the viscosity prefactor η_{ppv}, and Γ is the phase function as defined in Eq. (6). Table 2 lists all cases used in this study.

We use a method similar to that in (Zhong, 2006) to identify and quantify mantle plumes. At each depth, we find the maximum temperature T_{max}, the horizontally averaged temperature T_{ave} and the background temperature T_{bg} which is similar to T_{ave} but excludes cold downwellings with $T < T_{ave}$. The mantle plumes are defined as regions where the vertical velocity is positive and the temperature satisfies:

$$T > T_{bg} + f\,(T_{max} - T_{bg}), \tag{8}$$

where $f = 0.2$ sets the threshold for plume temperature. The plume heat flux is given by:

$$Q_{plume} = \int \delta T * u_z\, ds, \tag{9}$$

where $\delta T = T - T_{ave}$ is the plume temperature anomaly, u_z is the vertical velocity of the mantle plume, and the integral is for all plume regions at the same depth. The total dimensionless plume heat flux and CMB heat flux can be scaled to that of the 3D Earth by $Q_e = \rho_0 C_p \Delta T U_0 Q' \xi$, with Q' is dimensionless heat flux in our models, C_p is the heat capacity. $\xi = A/L$ is a correction factor for geometry difference, where A is the area for the Earth's surface or CMB, and $L = 3.0$ is the total lateral length of the 2D models.

3. Results

All our models start with a uniform layer of intrinsically dense material at the base of the box. Fig. 1 shows a series of snapshots in time for the temperature field (left column) and the composition field (right column) for case 1. Shortly after initiation, the intrinsically dense material is pushed to the middle of the box by cold downwellings, and forms a thermochemical pile above the CMB (i.e., Fig. 1d, f, h, j). For each case, the morphology of the thermochemical pile is quantified by calculating the areal fraction of CMB without pile material and the height of the pile. We define the height of the pile as the distance from the CMB where the lateral extent of the pile falls below 10% of the width of the box. The CMB heat flux and the plume heat flux at 300 km depth are also quantified for each case. Below, we first show the results for the reference case (case 1), and we then show how changes of model parameters affect the results.

3.1. Reference case

Case 1 uses a Rayleigh number of $Ra = 10^7$ and a buoyancy number of $B = 0.6$ (Table 2). Fig. 2a shows the time evolution of the height of the thermochemical pile and the areal fraction of CMB without pile material for this case. From t = 0 to t ~ 0.01, the height of the pile increases from 300 km to ~800 km. The evolution of the convection during this period, including pile formation, is significantly influenced by the initial conditions, but at later times the influences of initial conditions are lost and the intrinsic dynamics of the system take over.

After t ~ 0.01, the height of the pile begins to oscillate with time. The oscillation is mostly irregular, with both the magnitude and the period of the oscillation changing with time. However, we find that during t ~ 0.04–0.05, the height of the pile changes periodically. After t ~ 0.05, the oscillation of the pile height attenuates with time and after t ~ 0.06, the dynamics becomes more steady, without significant variation of the height of the pile. The long-term increase of areal fraction of CMB without pile material is due to the slow entrainment of pile material into the background mantle, which reduces the size of the pile. The evolution of the areal fraction of CMB without pile material correlates well with the evolution of the pile height during the period of t ~ 0.01–0.06, with correlation coefficients (denoted as r_1) of 0.61 and 0.78 during the time ranges of 0.01–0.04 and 0.04–0.06, respectively (Fig. 2a). A time evolution of the temperature and composition fields of case 1 is shown in Movie S1.

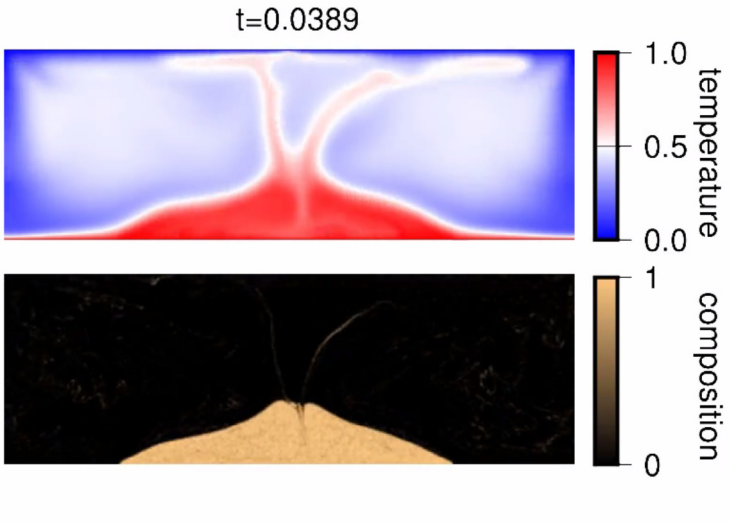

Movie S1. The evolution of temperature field (upper panel) and composition field (lower panel) for case 1. For full video refer the online version of the article.

Fig. 2b shows that, after t ~ 0.01, the evolution of the areal fraction of CMB without pile material also correlates well with the variation of the CMB heat flux, with correlation coefficients (denoted as r_2) of 0.80 and 0.95 during the time ranges of 0.01–0.04 and 0.04–0.06, respectively. These high correlations arise because the CMB heat flux is mainly released beneath the relatively cold regions outside of the pile

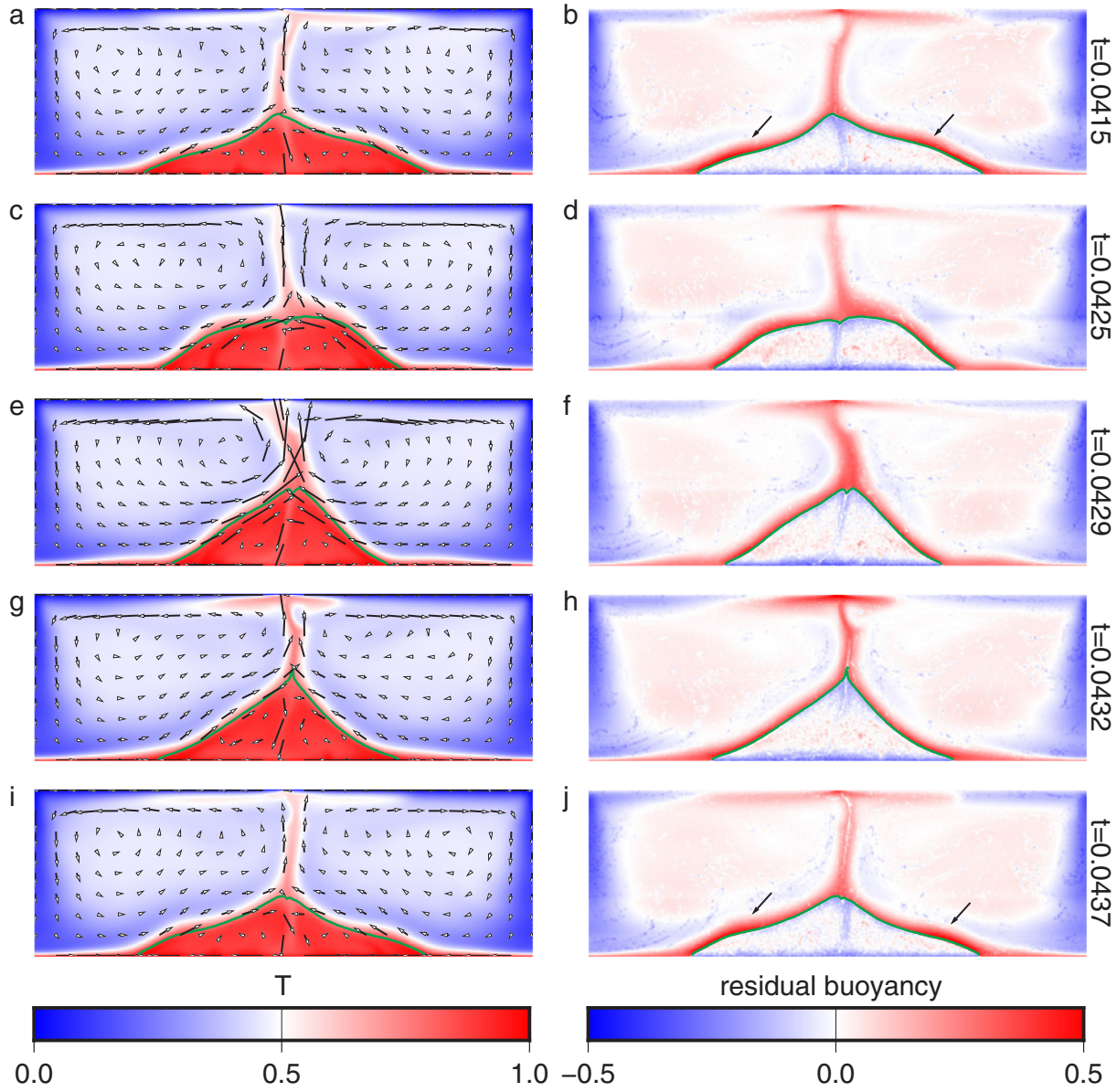

Fig. 3. Snapshots of temperature field (left) and the corresponding residual buoyancy field (right) for case 1 at t = 0.0415 (a, b), 0.0425 (c, d), 0.0429 (e, f), 0.0432 (g, h), and 0.0437 (i, j). The green lines mark the edges of the thermochemical pile. Arrows in the left panels show mantle flow velocity. (For interpretation of the references to colour in this figure legend, the reader is referred to the web version of this article.)

(Zhang and Zhong, 2011). The average areal fraction of CMB without pile material increases from ~0.4 at t = 0.01 to ~0.6 at t = 0.07. However, the magnitude of variation of CMB heat flux within each cycle is not coupled to the average areal fraction of CMB without pile material, but is instead controlled by the short-term variation of the areal fraction. The magnitude of CMB heat flux variation is generally small during time period of t ~ 0.01–0.04, but increases during time period of t ~ 0.04–0.05 with an increase of the variation of the areal fraction in CMB without pile material. After t ~ 0.06, there is little variation of CMB heat flux and little noticeable change of the pile morphology, although the average areal fraction of CMB without pile material is highest.

As shown in Fig. 2c, the plume heat flux at 300 km depth exhibits large amplitude pulses of activity, in contrast to the relatively smooth variations of CMB heat flux. Some of the plume pulses occur during CMB heat flux maxima. However, the plume heat flux pulses often occur during the decrease phase of the CMB heat flux, especially during time period of t ~ 0.04–0.05, when the pulses of plume heat flux are regularly spaced in time and the variations of CMB heat flux are nearly periodic. Similar to the variation of CMB heat flux, measures of plume activities (e.g., the occurrence and the magnitude of the pulse of plume heat flux) are not coupled with the long-term increase of the areal fraction of CMB without pile material.

Why are the changes in pile morphology, CMB heat flux and pulses of plume heat flux regular and periodic at some times, and irregular at others? To answer this question, we examine the interactions between the plumes and the thermochemical pile that lead to variations of CMB heat flux and plume heat flux. Fig. 3 shows a series of snapshots in time of the temperature field (left column) and the residual buoyancy field (right column) for case 1 from t = 0.0415 to 0.0437, illustrating the

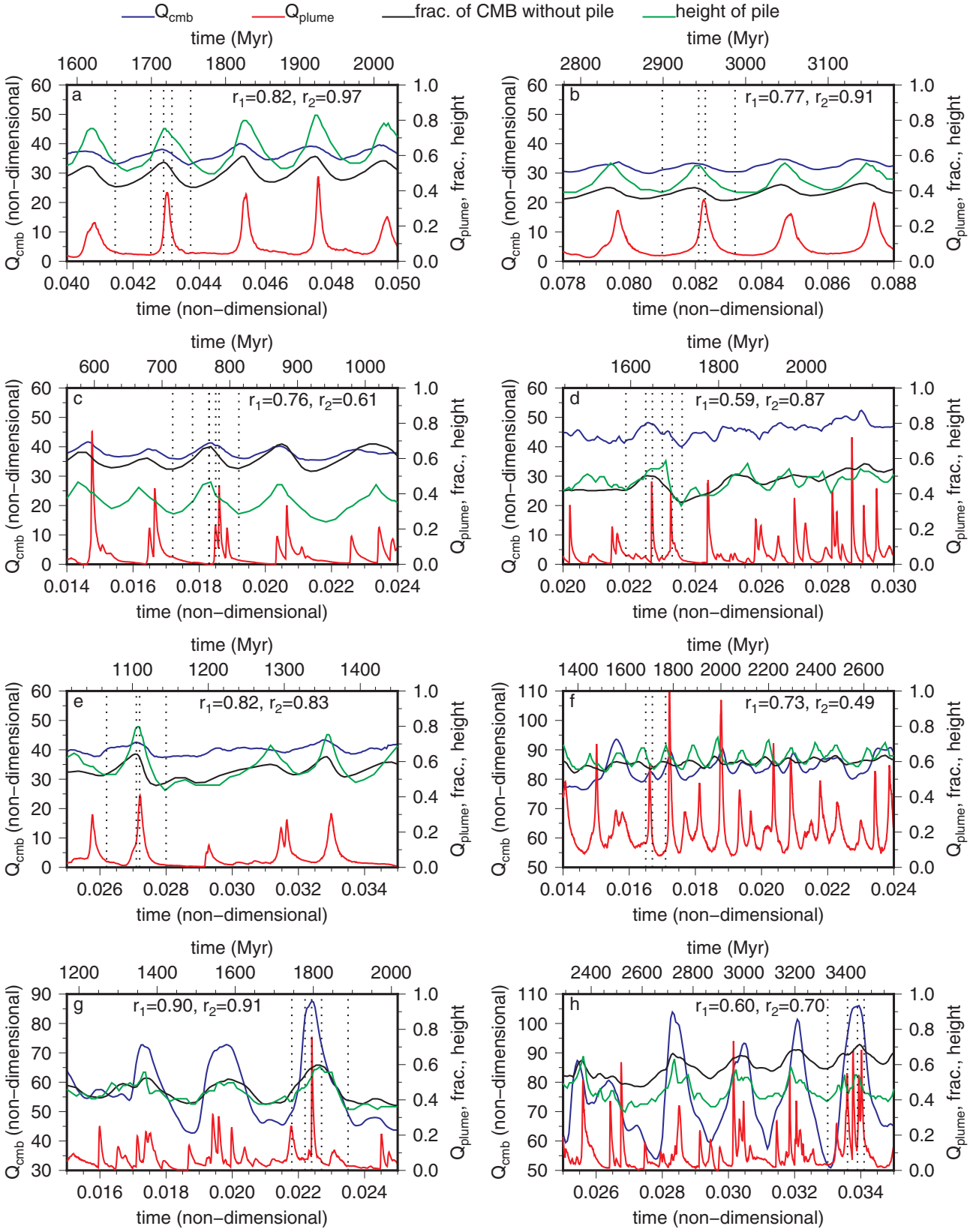

Fig. 4. Time evolution of global CMB heat flux (Q_{cmb}), plume heat flux at 300 km depth (Q_{plume}, normalized with a non-dimensional reference value of 180), areal fraction of the CMB without pile material and the height of the pile for case 1 (a), case 2 (b), case 3 (c), case 4 (d), case 5 (e), case 6 (f), case 7 (g) and case 8 (h). r_1 and r_2 are the correlation efficiencies for the correlations between the height of the pile and the areal fraction of CMB without pile material, and between the areal fraction of CMB without pile material and the CMB heat flux, respectively.

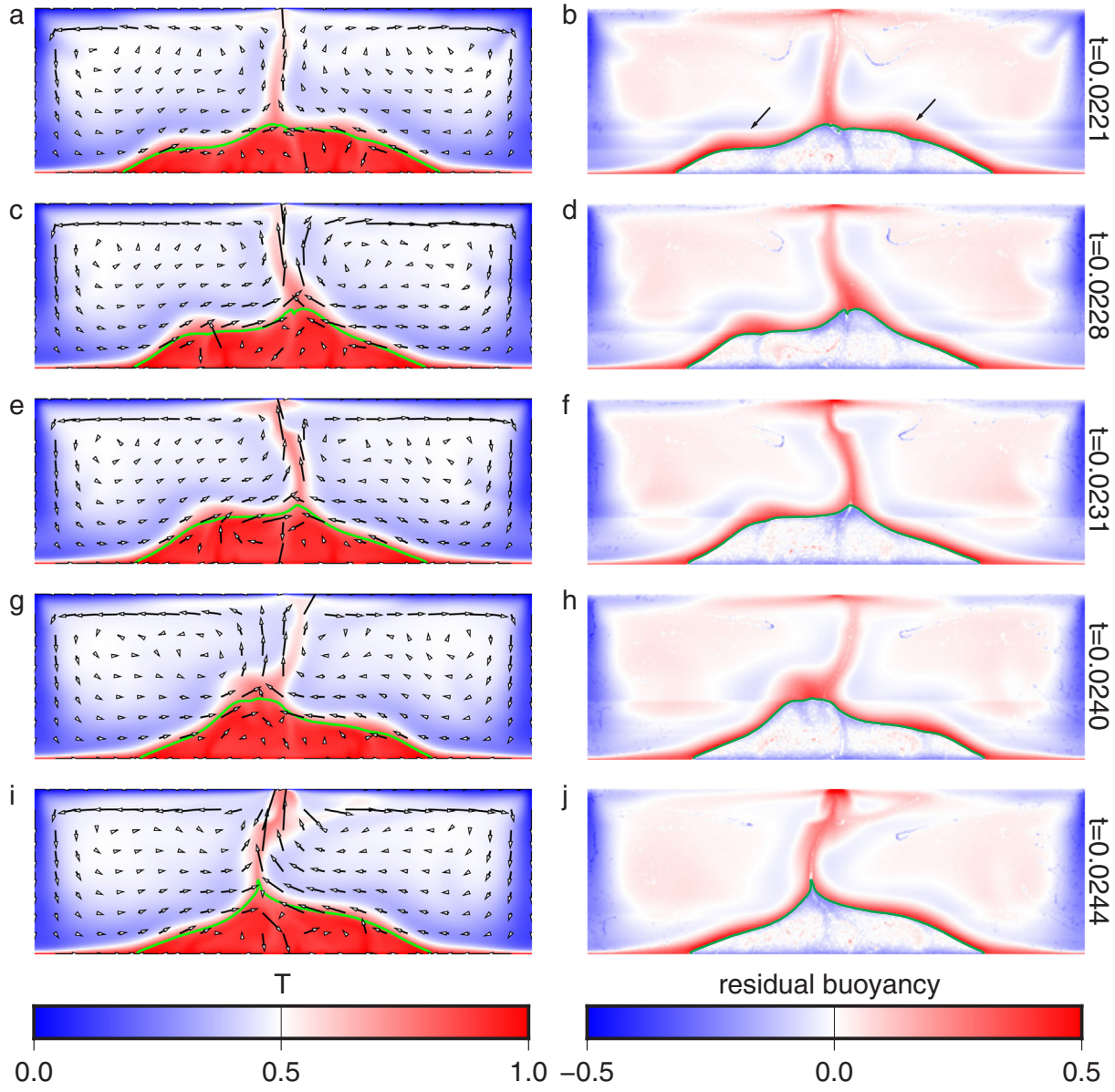

Fig. 5. Snapshots of temperature field (left) and the corresponding residual buoyancy field (right) for case 1 at t = 0.0221 (a, b), 0.0228 (c, d), 0.0231 (e, f), 0.0240 (g, h), and 0.0244 (i, j). The green lines mark the edges of the thermochemical pile. Arrows in the left panels show mantle flow velocity. (For interpretation of the references to colour in this figure legend, the reader is referred to the web version of this article.)

dynamics during one periodic cycle. At t = 0.0415, a weak thermal plume conduit extends from the top of the pile to near the surface. Thermal anomalies form on both sides of the pile and lead to large positive buoyancy in the regions indicated by black arrows in Fig. 3b. From t = 0.0415 to t = 0.0425, the thermal anomalies on each side of the pile migrate simultaneously towards the crest of the pile, while at the same time, the temperature of the plume decreases. At t = 0.0429, the thermal anomalies merge at the crest of the pile and the plume strengthens. At t = 0.0432, the strengthened plume rises rapidly to near the surface through the pre-existing plume conduit (Fig. 3g) and the large positive residual buoyancy at the crest of the pile is reduced (Fig. 3h).

The height of the pile increases during the plume strengthening between t = 0.0415 and t = 0.0425, and at t = 0.0432 it reaches its maximum. After that, the pile collapses and the height of the pile decreases. At t = 0.0437, the height of the pile is reduced to its minimum and the morphology of the pile returns to its shape at t = 0.0415, with formation of thermal anomalies resulting in large positive residual buoyancy on each side of the pile (indicated by black arrows in Fig. 3j), thus renewing the cycle.

In summary, we show in Fig. 3 that the thermal anomalies at both edges of the pile merge at the crest of the pile, and form a strong plume there. The pile is significantly elevated during the formation of the plume. As the plume rises toward the surface, the pile starts to collapse. As shown in Fig. 4a, during t ~ 0.04–0.05, the CMB heat flux decreases by ~10–15% between the maximum and the minimum of each cycle, whereas the peaks of the plume heat flux are about 5 times larger than the background value. In addition, it takes more time for the CMB area without pile material and the CMB heat flux to increase to peaks than to decrease to troughs, indicating that the pile grows more slowly than it

collapses.

We now focus on the dynamics with irregular, aperiodic variations of pile morphology and CMB heat flux, and irregular pulses of plume heat flux. As an example of this behavior, Fig. 5 shows a series of snapshots in time of the temperature field (left column) and the residual buoyancy field (right column) for case 1 from t = 0.0221 to 0.0244, including irregular, aperiodic variations. At t = 0.0221, a weak thermal plume rises from the crest of the thermochemical pile to beneath the upper surface. The pile has an asymmetric shape, with the left side of the pile less elevated than the right side. Hot thermal anomalies are found on both sides of the pile, which cause large positive residual buoyancy on the pile edges (again indicated by black arrows in Fig. 5b). At t = 0.0228, the thermal anomaly on the right side of the pile forms a strong thermal plume at the crest of the pile, and the pile is slightly elevated beneath the plume. As this plume continues to rise toward the upper surface at t = 0.0231, the elevated part of the pile collapses.

The thermal anomaly on the left side of the pile migrates towards the crest of the pile from t = 0.0221 to t = 0.0240. By t = 0.0240, the thermal anomaly has evolved into a strong thermal plume at the top of the pile with large positive residual buoyancy in the plume region, and the pile is slightly elevated beneath the plume. The plume rises to near the upper surface by t = 0.0244, while the positive residual buoyancy at the crest of the pile decreases, and by t = 0.0244 the elevated part of the pile has collapsed.

In summary, Fig. 5 shows the formation of two successive strong thermal plumes from thermal anomalies on the pile edges. Although we do not observe significant global change of the pile morphology, our results show that the formation of each thermal plume locally elevates the pile, and as the plume rises towards the surface, the elevated part of the pile collapses.

simultaneously, enhancing the time variations of pile morphology and global CMB heat flux.

3.2. Influence of model parameters

The influences of physical parameters of the mantle on the CMB heat flux, pile morphology and plume formation have been widely explored in previous studies (e.g., Deschamps and Tackley, 2008, 2009; Nakagawa and Tackley, 2011; Li et al., 2014b). It is well established that the morphology of thermochemical piles, the formation of mantle plumes and the magnitude of CMB heat flux are sensitive to the intrinsic density and volume of the pile material (e.g., the buoyancy number), the Rayleigh number and the ppv phase transition (Deschamps and Tackley, 2009; Nakagawa and Tackley, 2011; Li et al., 2014b). In this section, we focus on understanding how variations of these parameters affect our results.

In case 2, the buoyancy number of the intrinsic dense material is increased to $B = 0.8$. Because of increased density of the thermochemical pile, the morphology of the pile does not change as much as that in case 1, and the magnitudes of the height of pile, the areal fraction and the CMB heat flux are all lower than in case 1 (Fig. 4b). The dynamics (shown in Movie S2) is generally similar to that in case 1, with the formation of thermal plumes leading to morphologic changes of the thermochemical pile, which in turn causes variation of CMB area covered by pile material and variation of CMB heat flux. As an example, Fig. 6 shows a series of snapshots in time of the temperature field for case 2 from t = 0.0810 to 0.0832, illustrating that the height of the pile and the lateral extent of the pile are significantly affected by the formation of a strong thermal plume, which is similar to that shown in Fig. 3 for case 1.

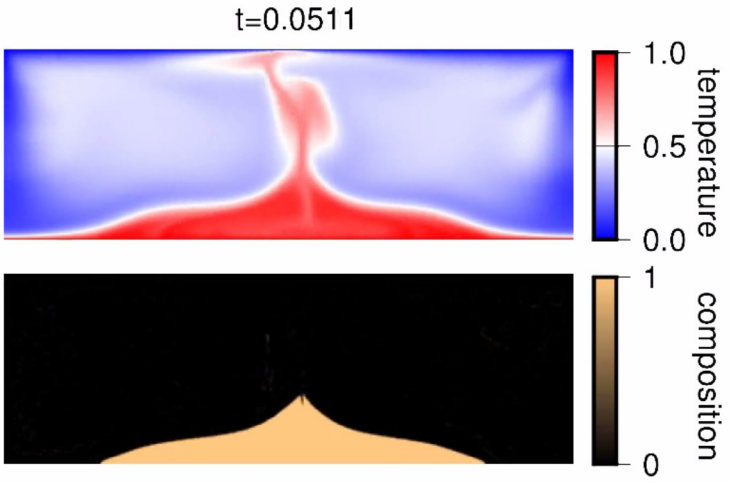

Movie S2. The evolution of temperature field (upper panel) and composition field (lower panel) for case 2. For full video refer the online version of the article.

The processes involving interaction between thermal plumes and the thermochemical pile occur, and are most clearly illustrated, during times with periodic behavior (Fig. 3). Even so, the periodic behavior and aperiodic behavior represent different expressions of the same basic physical processes. During aperiodic behavior, the two sides of the pile are typically in different phases of the growth/collapse cycle, due to the formation of separate plumes on each side of the pile at different times, whereas during periodic behavior, simultaneous plume development causes the left and right sides of the pile to grow and collapse

In case 3, the initial thickness of the global layer of intrinsically dense material is reduced to 150 km, while other parameters are the same as case 1. Compared to case 1, the pile in case 3 has smaller size and lower height, and the areal fraction of CMB without pile material is correspondingly larger (Fig. 4c). The pile stays on the CMB for less amount of time before being completely stirred into the background mantle (Movie S3). Fig. 4c shows the evolution of the CMB heat flux, areal fraction of CMB without pile material and pulses of plume heat flux from t = 0.014 to 0.024, when all are changing periodically.

Within each periodic cycle, several pulses of plume heat flux occur during the decrease phase of the CMB heat flux. Between t = 0.018 and 0.019, the pulses of plume heat flux occur close to the time when the CMB heat flux reaches a minimum value, in contrast to cases 1 and 2 in which the pulses of plume heat flux occur shortly after the CMB heat flux reaches a maximum value, and long before the CMB heat flux reaches minimum.

In case 4, we increase the Rayleigh number to $Ra = 3 \times 10^7$ (3× of that in case 1) while keeping other parameters the same as in case 1. As expected, the convection is more chaotic than case 1 (Movie S4). The CMB heat flux is higher than in case 1 (Fig. 4d), as expected for convection with a higher Rayleigh number, but the magnitude of its oscillation is not very different from case 1. As shown in Movie S4 and Fig. 8, there are often more than two plumes on top of the thermo-

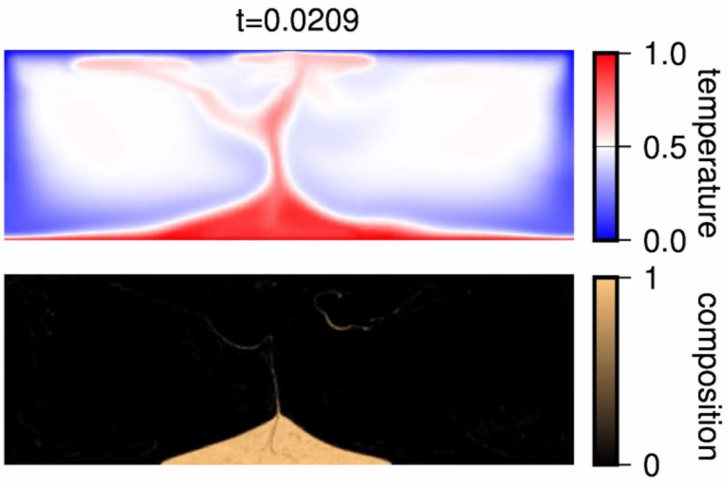

Movie S3. The evolution of temperature field (upper panel) and composition field (lower panel) for case 3. For full video refer the online version of the article.

We further show in Fig. 7 a series of snapshots of the temperature field for case 3 from t = 0.0172 to 0.0192, illustrating the origin of three pulses of plume heat flux during this period. We find that the chemical pile. The formation of multiple plumes leads to localized morphologic change of the pile, which is similar to that shown in Fig. 5 for case 1.

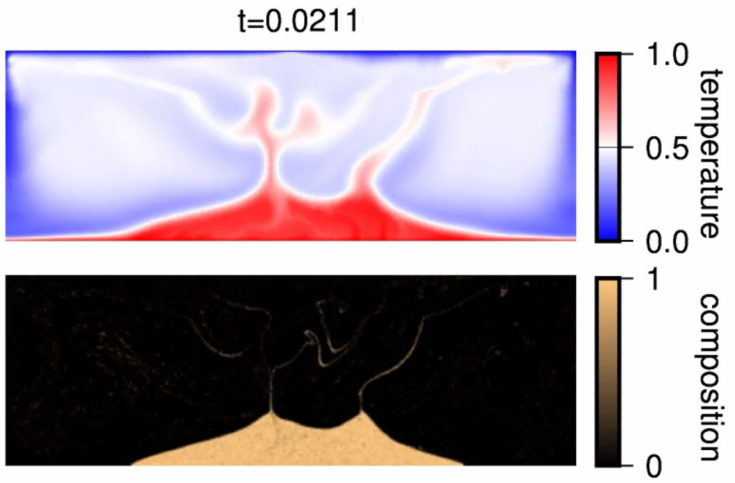

Movie S4. The evolution of temperature field (upper panel) and composition field (lower panel) for case 4. For full video refer the online version of the article.

morphologic change of the pile is caused by the formation and rise of multiple plumes. Compared to cases 1 and 2, plumes in case 3 travel for longer distance from the top of the pile to near the surface since the height of the pile is lower in case 3. In addition, plumes in Fig. 7 rise through the viscous background mantle to near the surface, different from plumes that rise through the pre-existing hot plume conduits (e.g., Figs. 3 and 5) and avoiding the viscous background mantle.

In cases 5, 6, 7 and 8, we explore the effects of the ppv phase transition. The model parameters for case 5 are the same as case 1 except that case 5 includes a 1% density increase for the ppv phase. The changes of CMB heat flux, height of pile and areal fraction of pile are less regular as that in case 1 (Fig. 4e), which may be because the additional negative buoyancy in the ppv phase slightly changes the convection pattern. The CMB heat flux is slightly higher than case 1, but

the magnitude of CMB heat flux oscillation is similar for both cases (Fig. 4e). As shown in Fig. 9 and Movie S5, the morphology of the pile is significantly affected during the formation and rise of thermal plumes.

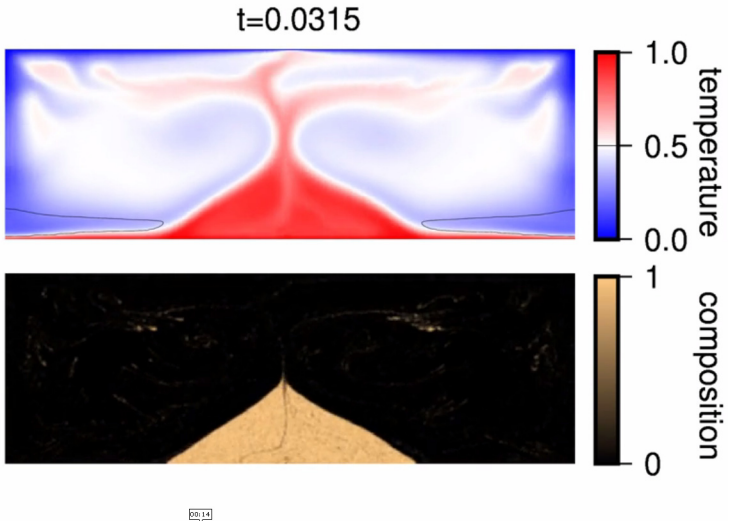

Movie S5. The evolution of temperature field (upper panel) and composition field (lower panel) for case 5. For full video refer the online version of the article.

In addition to the density increase, the viscosity of the ppv phase in case 6 is decreased by 100 times. Accordingly, the convection becomes more chaotic, and the pile morphology, CMB heat flux and plume heat flux vary more rapidly than in previous cases (Fig. 4f). The CMB heat flux is higher than previous cases (Fig. 4f), which leads to higher mantle temperatures (Movie S6). The pulses of plume heat flux during the time period of t = 0.014–0.024 are frequent and nearly evenly-spaced, but they are not accompanied by significant changes of the height of the pile (Fig. 4f). This is because the pile remains in an 'elevated' phase due to the frequent formation of strong plumes from both sides of the pile, such as that shown in Fig. 10.

To further investigate how the changes of ppv volume affect the CMB heat flux, we decrease T_{ppv} to 0.39 in case 7 while keeping the other parameters the same as case 6. Since the temperature required for the ppv phase transition in case 7 is lower than that in case 6, the volume of ppv phase in case 7 is, in general, smaller than that in case 6 (Movie S7). We find that the CMB heat flux in ppv regions is much higher than other regions, because the low viscosity of ppv regions thins the basal thermal boundary layer there. Compared to case 6, the CMB heat flux in case 7 is generally lower due to small volume of the less viscous ppv phase, but the fluctuation of CMB heat flux is higher (Fig. 4 g), due to the larger variation of ppv volume with time (Fig. 11). Again, we find that the morphology of the pile is significantly altered

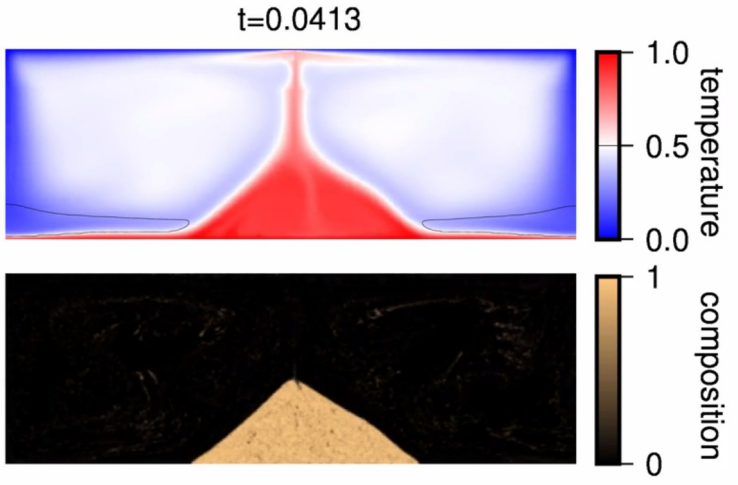

Movie S6. The evolution of temperature field (upper panel) and composition field (lower panel) for case 6. For full video refer the online version of the article.

during the formation and the ascent of thermal plumes (Movie S7), and an example is shown in Fig. 11.

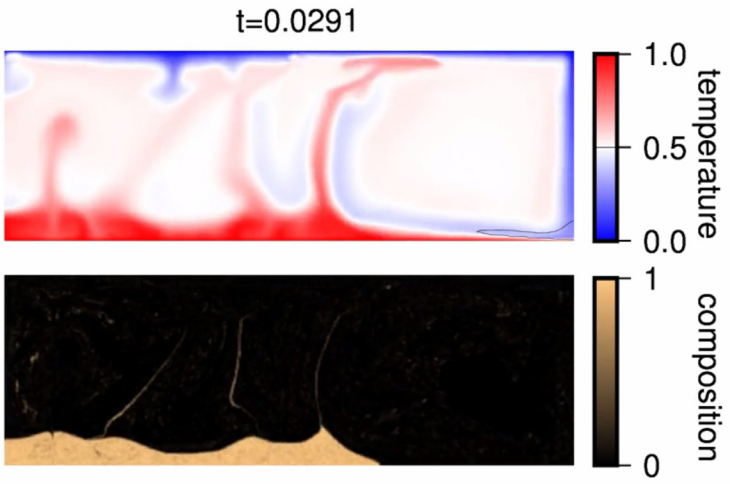

Movie S7. The evolution of temperature field (upper panel) and composition field (lower panel) for case 7. For full video refer the online version of the article.

We further reduce the viscosity of ppv in case 8 such that the ppv phase is 1000 times less viscous than the pv phase. With this reduction of ppv viscosity, the CMB heat flux in case 8 is generally higher than in case 7 (Fig. 4h). In addition, plumes form more frequently than in case 7 (Fig. 4h). From t ~ 0.025 to ~0.035, the CMB heat flux changes quasi-periodically and multiple pulses of plume heat flux clustered around the peaks of CMB heat flux (Fig. 4h). Although the change of areal fraction of CMB without pile is relatively small, the CMB heat flux exhibits significant oscillations during this period. This is because the CMB heat flux is very sensitive to the amount of ppv phase present, and small changes of ppv volume due to changes of pile morphology lead to large variations of CMB heat flux. Nevertheless, the morphology of the pile is significantly affected during the formation of mantle plumes, as shown in Fig. 12 and Movie S8.

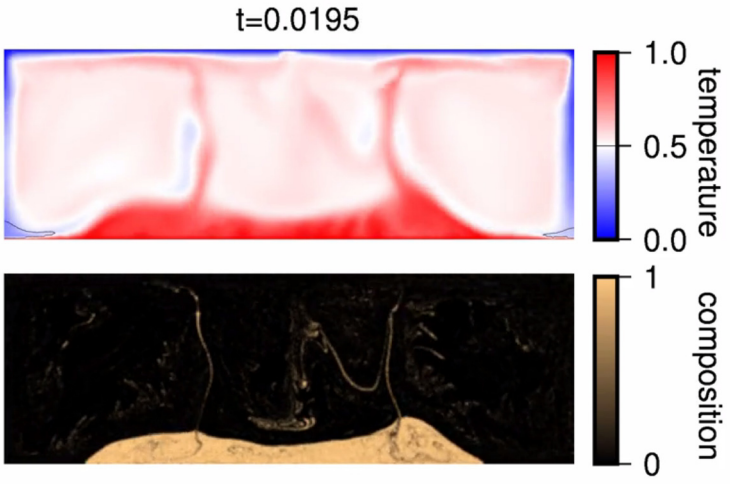

Movie S8. The evolution of temperature field (upper panel) and composition field (lower panel) for case 8. For full video refer the online version of the article.

For better comparison, we summarize the evolution of CMB heat flux for cases 1, 2, 3, 4, and 8 in Fig. 13. Compared to case 1 (black curve), as we increase the buoyancy number of the intrinsically dense material in case 2, the CMB heat flux decreases (red curve) because the thermochemical pile covers larger areal fraction of CMB. We reduce the initial volume of the intrinsically dense material by two times in case 3. As a result, the size of pile is smaller and covers less CMB area in case 3 than case 1, which is consistent with that the CMB heat flux in case 3 (blue curve) is higher than case 1. The CMB heat flux also increases as we increase the Rayleigh number in case 4 (green curve). The CMB heat flux is significantly increased by the presence of weak ppv phase in the lowermost mantle, and it varies in time by up to ~50% for case 8 (purple curve) in which the viscosity in regions with ppv phase is reduced by 1000 times. In all cases, the magnitude of CMB heat flux variation is time-dependent due to changes of convection pattern.

In summary, we find that in all cases, the formation of thermal plumes typically leads to increases in height of the pile, and the pile collapses as the plumes rise toward the surface. The morphologic change of the pile causes variation of CMB heat flux. A strong correlation between the areal fraction of CMB without pile and the CMB heat flux is observed in all calculations (Figs. 2 and S1–S7, with the correlation coefficients shown in each figure). It needs to be emphasized that

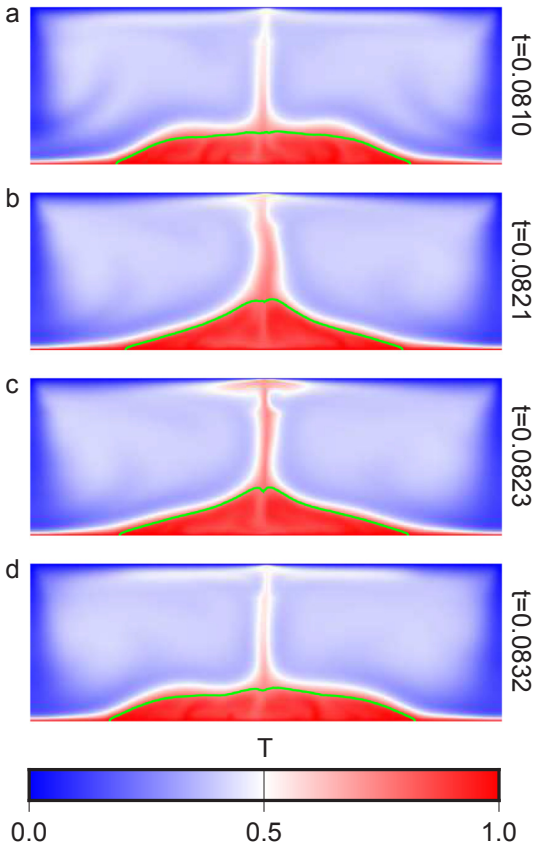

Fig. 6. Snapshots of temperature field for case 2 at t = 0.0810 (a), 0.0821 (b), 0.0823 (c) and 0.0832 (d). The green lines mark the edges of the thermochemical pile. The global CMB heat flux, plume heat flux at 300 km depth, areal fraction of the CMB without pile material and the height of the pile at each time are shown in Fig. 4b with the vertical dotted lines in Fig. 4b marking the time for each selected snapshot. The buoyancy number for the intrinsic dense material is increased to $B = 0.8$ in case 2. (For interpretation of the references to colour in this figure legend, the reader is referred to the web version of this article.)

the convection pattern changes significantly throughout the calculation for each case (Figs. 3 and 5), and varies case by case (Figs. 6–12). We observe temporarily periodic variations of pile morphology, CMB heat flux and plume heat flux in some cases (e.g., cases 1, 2, 3 and 8, Fig. 4), but these periodic behaviors are not guaranteed and they could disappear due to a relatively small change of convection pattern. Nevertheless, the basic physical process for the interaction between piles and plumes occurs universally in our models.

4. Discussion

4.1. Linking the morphology of thermochemical piles to mantle plume formation and CMB heat flux

Our numerical models focus on the interaction between mantle plumes and thermochemical piles of large-scale compositional heterogeneities in the lowermost mantle, and its consequences for the pile morphology and CMB heat flux. We find good correlations among the height of thermochemical pile, the areal fraction of CMB without pile material and the CMB heat flux in all cases. The heat flux delivered by mantle plumes can change significantly and episodically with time (e.g., Figs. 2c and 4), consistent with previous studies (Lin and van Keken, 2005).

Our models indicate that the morphology of thermochemical piles in the lower mantle can significantly change during the formation and the ascent of mantle plumes, which in turn causes time variation of CMB heat flux. This process is best illustrated by the periodic and concurrent variations of pile morphology, CMB heat flux and plume heat flux in some cases. The mechanism that causes these variations is similar to that proposed by Olson and Amit (2015). The formation of a strong mantle plume from thermal anomalies on the margins of the thermochemical pile provides large positive residual buoyancy, elevating the pile. As the strong plume rises towards the surface, the large positive residual buoyancy on the pile edges decreases and the pile collapses. The collapse of the pile on the CMB results in thermal insulation of the core and with that, a reduction of CMB heat flux. In this scenario, the CMB heat flux changes as a result of morphologic change of the thermochemical pile, and the pile changes morphology because of the formation of mantle

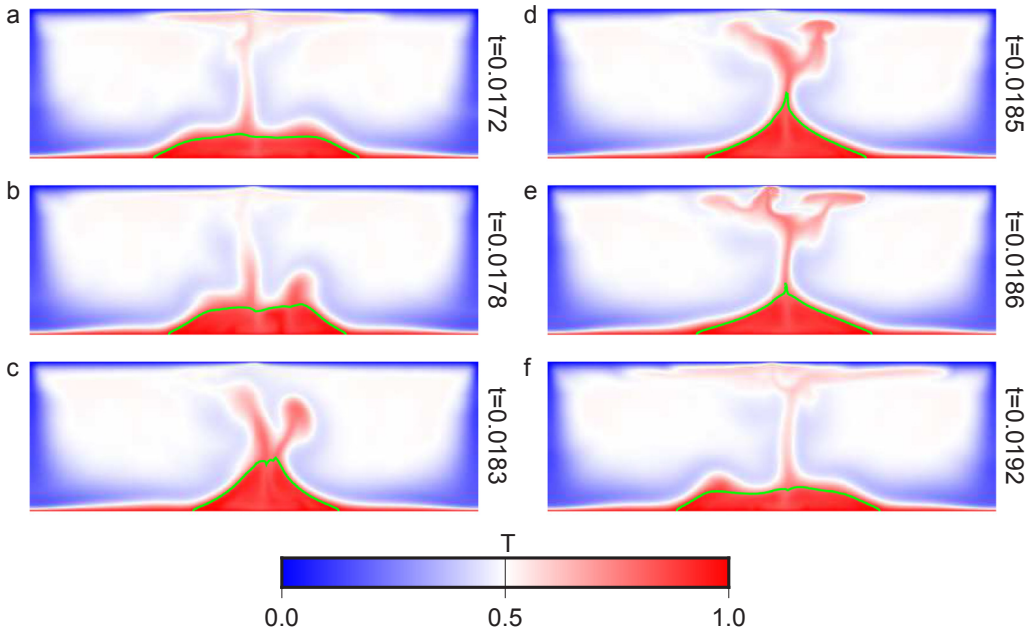

Fig. 7. Snapshots of temperature field for case 3 at t = 0.0172 (a), 0.0178 (b), 0.0183 (c), 0.0185 (d), 0.0186 (e), and 0.0192 (f). The green lines mark the edges of the thermochemical pile. The global CMB heat flux, plume heat flux at 300 km depth, areal fraction of the CMB without pile material and the height of the pile at each time are shown in Fig. 4c with the vertical dotted lines in Fig. 4c marking the time for each selected snapshot. The initial thickness of the global layer of intrinsically dense material is 150 km for case 3. (For interpretation of the references to colour in this figure legend, the reader is referred to the web version of this article.)

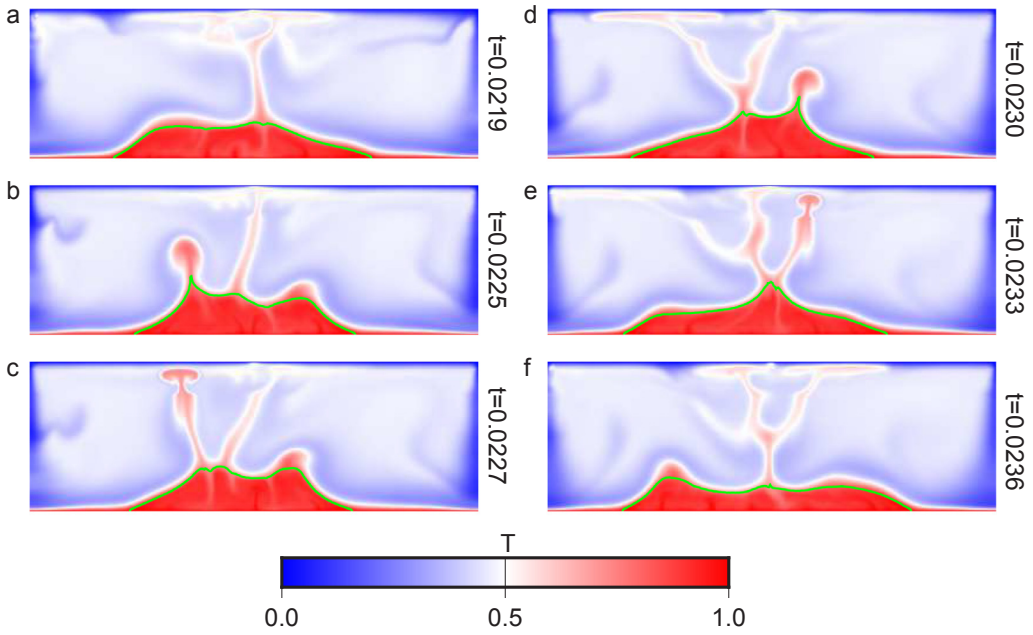

Fig. 8. Snapshots of temperature field for case 4 at t = 0.0219 (a), 0.0225 (b), 0.0227 (c), 0.0230 (d), 0.0233 (e), and 0.0236 (f). The green lines mark the edges of the thermochemical pile. The global CMB heat flux, plume heat flux at 300 km depth, areal fraction of the CMB without pile material and the height of the pile at each time are shown in Fig. 4d with the vertical dotted lines in Fig. 4d marking the time for each selected snapshot. The Rayleigh number is Ra = 3e7 for case 4. (For interpretation of the references to colour in this figure legend, the reader is referred to the web version of this article.)

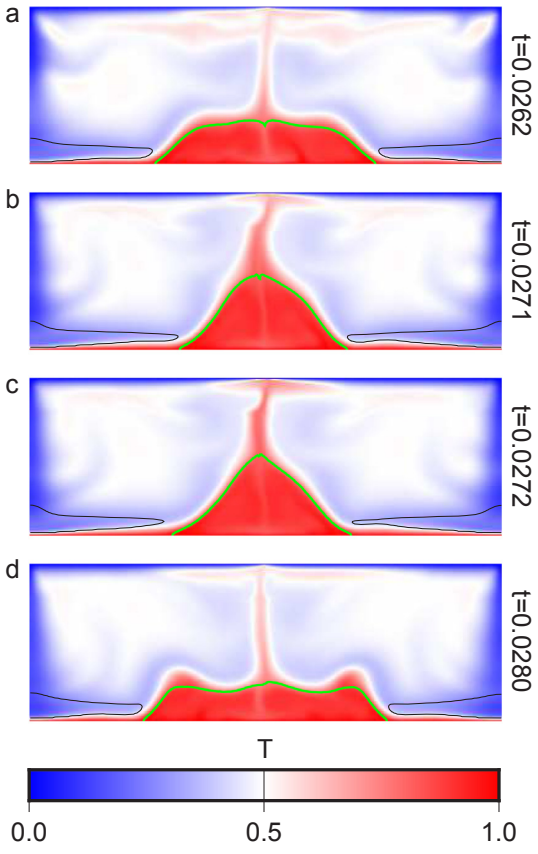

Fig. 9. Snapshots of temperature field for case 5 at t = 0.0262 (a), 0.0271 (b), 0.0272 (c), and 0.0280 (d). The green lines mark the edges of the thermochemical pile. The black lines mark the boundary of the ppv phase. The global CMB heat flux, plume heat flux at 300 km depth, areal fraction of the CMB without pile material and the height of the pile at each time are shown in Fig. 4e with the vertical dotted lines in Fig. 4e marking the time for each selected snapshot. We introduce ppv phase transition in case 5. In this case, the ppv is 1% denser than the pv phase, but both phases have the same viscosity. (For interpretation of the references to colour in this figure legend, the reader is referred to the web version of this article.)

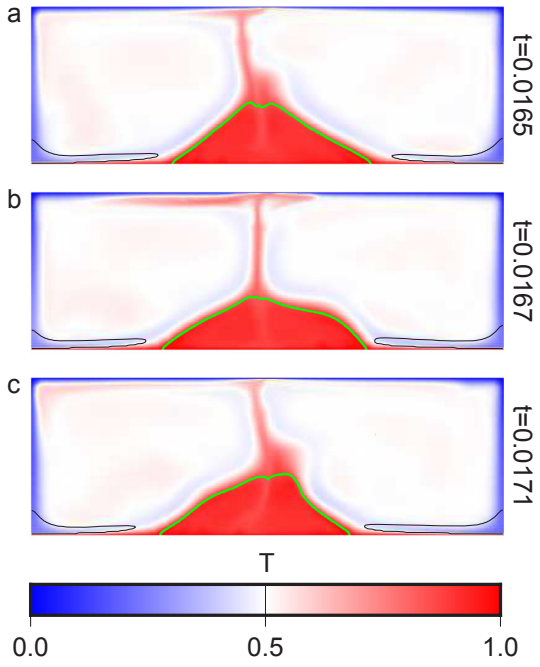

Fig. 10. Snapshots of temperature field for case 6 at t = 0.0165 (a), 0.0167 (b), and 0.0171 (c). The green lines mark the edges of the thermochemical pile. The black lines mark the boundary of the ppv phase. The global CMB heat flux, plume heat flux at 300 km depth, areal fraction of the CMB without pile material and the height of the pile at each time are shown in Fig. 4f with the vertical dotted lines in Fig. 4f marking the time for each selected snapshot. The ppv phase is 100 times less viscous than the pv phase in case 6. (For interpretation of the references to colour in this figure legend, the reader is referred to the web version of this article.)

plumes. Thus, repeated formation of mantle thermal plumes on pile flanks seems to be the driving force for these time variations.

During times of periodic behavior, the CMB heat flux, plume heat flux, and both sides of the thermochemical pile change coherently (e.g., Fig. 3). Thermal anomalies forming on both sides of the pile merge to

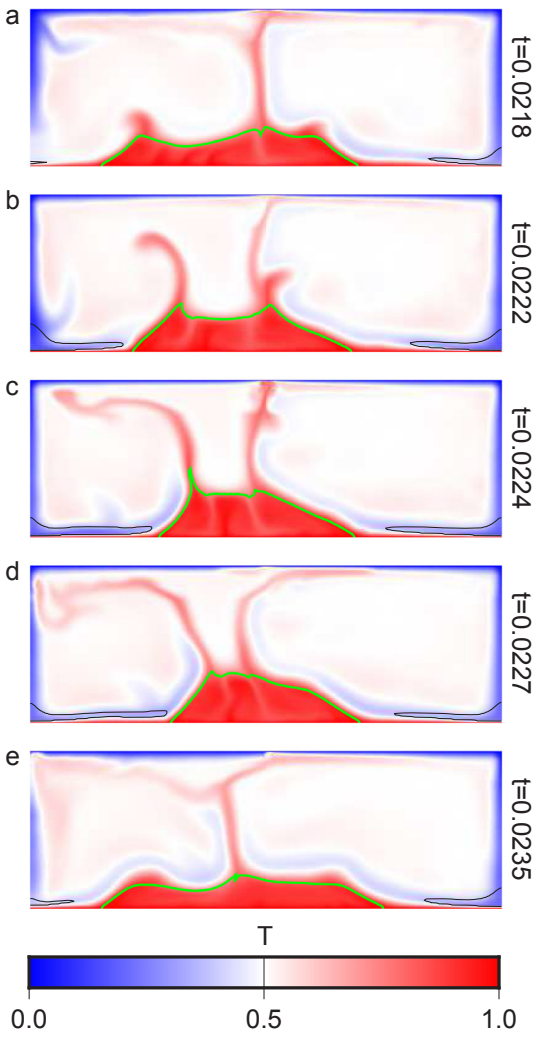

Fig. 11. Snapshots of temperature field for case 7 at t = 0.0218 (a), 0.0222 (b), 0.0224 (c), 0.0227 (d) and 0.0235 (e). The green lines mark the edges of the thermochemical pile. The black lines mark the boundary of the ppv phase. The global CMB heat flux, plume heat flux at 300 km depth, areal fraction of the CMB without pile material and the height of the pile at each time are shown in Fig. 4 g with the vertical dotted lines in Fig. 4 g marking the time for each selected snapshot. In case 7, we use T_{ppv} = 0.39 for the ppv phase transition, and the ppv phase is 100 times less viscous than the pv phase. (For interpretation of the references to colour in this figure legend, the reader is referred to the web version of this article.)

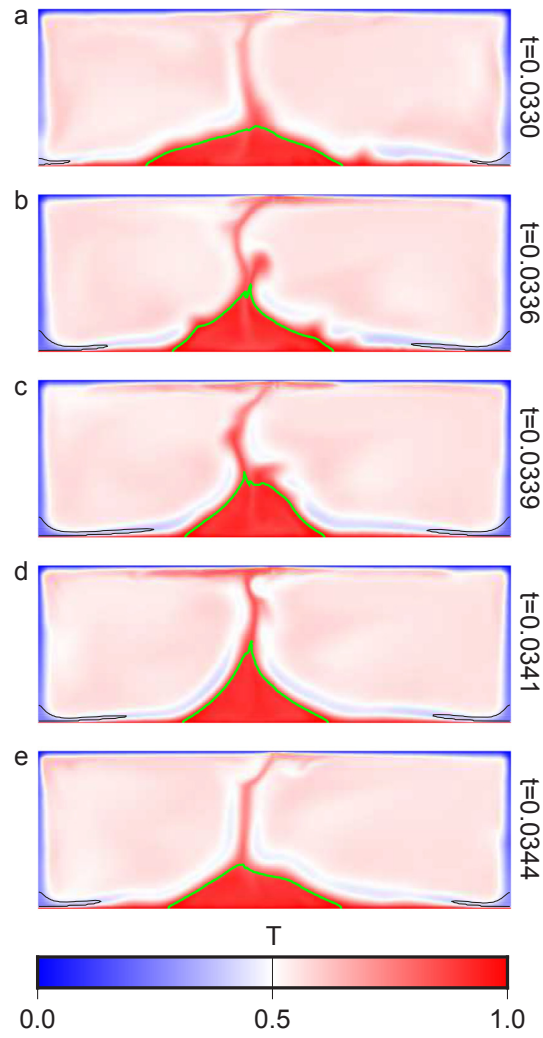

Fig. 12. Snapshots of temperature field for case 8 at t = 0.0330 (a), 0.0336 (b), 0.0339 (c), 0.0341 (d) and 0.0344 (e). The green lines mark the edges of the thermochemical pile. The black lines mark the boundary of the ppv phase. The global CMB heat flux, plume heat flux at 300 km depth, areal fraction of the CMB without pile material and the height of the pile at each time are shown in Fig. 4 h with the vertical dotted lines in Fig. 4 h marking the time for each selected snapshot. In case 8, we use T_{ppv} = 0.39 for the ppv phase transition, and the ppv phase is 1000 times less viscous than the pv phase. (For interpretation of the references to colour in this figure legend, the reader is referred to the web version of this article.)

form a strong plume at the crest of the pile. The pulses of plume heat flux near the surface occur slightly after the peaks of CMB heat flux, but well before the next CMB heat flux minimum (e.g., Fig. 4a). However, during times of aperiodic behavior, plumes form at different times on the pile sides, and the individual plumes only change the pile morphology locally (e.g., Fig. 5). In that situation, there is no clear link between the pulses of plume heat flux and the variation of the global CMB heat flux (e.g., Fig. 2c).

Mineral physics studies suggest that the ppv phase could be 5–1000 times less viscous than the pv phase (Hunt et al., 2009; Ammann et al., 2010), although a higher viscosity of the ppv phase than the pv phase has also been proposed (Karato, 2010). Here, we explored the effects of weak (low viscosity) ppv phase transition on our result. We find that the frequency of mantle plume formation, the CMB heat flux and its magnitude of oscillation are all significantly increased by the presence of weak ppv phase in cold regions of the lowermost mantle. The presence of weak ppv phase also leads to increase of the entrainment rate of the thermochemical piles, similar to that found by (Li et al., 2014b). However, it needs to be emphasized that the long-term stability of thermochemical piles is also controlled by other factors such as the intrinsic dense of the pile material. The effects of weak ppv on increasing the instability of piles could be compensated by increasing the intrinsic density of the pile.

Our models include numerous simplifications. For example, there is only one thermochemical pile in our models, and we assume 2D geometry. It is expected that the 3D mantle dynamics is more complex, and accordingly our models should also become more complex if we were to increase the aspect ratio or adopt 3D spherical geometry. However, our purpose here is not to model all of Earth's complexity, but rather to illustrate basic interactions between mantle plumes and thermochemical piles and the influence of these interactions on the CMB heat flux. Consequently, we have focused on models with minimum complexity.

Nevertheless, we can speculate on how these additions might affect our results. For example, were we to increase the aspect ratio of these models, two or more isolated piles are expected to form along the bottom boundary, and in that situation, changes in the piles would need to be in phase to optimally affect the CMB heat flux. Plumes often form

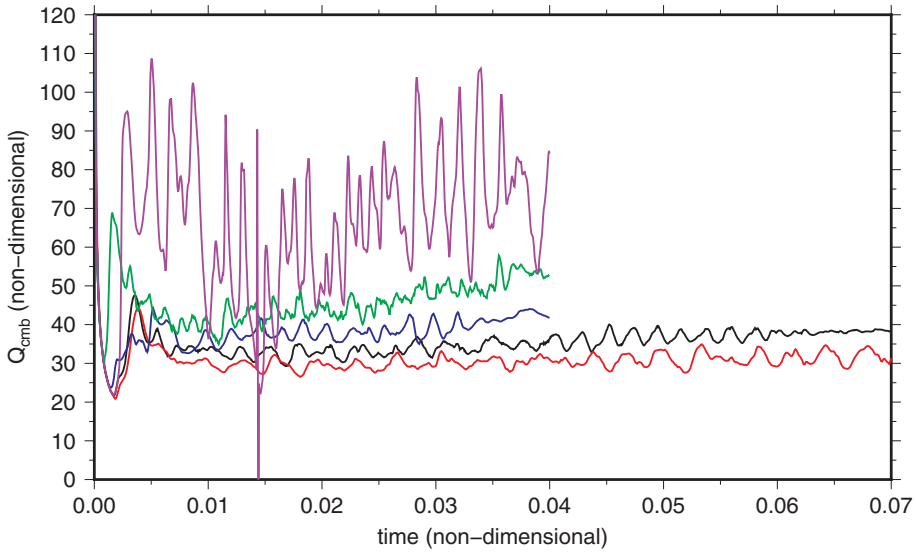

Fig. 13. The time evolution of global CMB heat flux for case 1 (black curve), case 2 (red curve), case 3 (blue curve), case 4 (green curve) and case 8 (purple curve). (For interpretation of the references to colour in this figure legend, the reader is referred to the web version of this article.)

on top of the crest of the middle of thermochemical piles in our 2D models which is due to the small lateral extent of the piles. In contrast, previous 3D geodynamic modeling results show that thermal plumes form preferentially near the edges of the thermochemical piles (Tan et al., 2011; Li and Zhong, 2017). We can apply our 2D modeling results to understand the interaction between plumes and the edges of piles in 3D models. Plumes in 3D models also have smaller size compared to the whole mantle than that in 2D models. Therefore, our 2D models suggest that several strong mantle plumes need to form in unison in order to elevate an entire pile and to substantially change the CMB heat flux, particularly when 3D effects are factored in.

4.2. Implications on the connection between superchrons and LIP events

The repetitive occurrence of geomagnetic superchrons during the Phanerozoic, and the concurrence of the latest superchron (e.g., the CNS) and the peak of pulses of LIP events in the mid-Cretaceous have generated much speculation on possible links between the lowermost mantle structure, the formation of mantle plumes, the CMB heat flux, and the frequency of geomagnetic polarity reversals (Larson and Olson, 1991; Haggerty, 1994; Larson and Kincaid, 1996; Courtillot and Olson, 2007; Zhang and Zhong, 2011; Biggin et al., 2012; Olson and Amit, 2015). Some early studies proposed that the formation of mantle plumes from the D″ layer increases the CMB heat flux and the outer core activity which stabilize non-reversing magnetic fields and result in superchrons (Larson and Olson, 1991; Haggerty, 1994). However, this hypothesis is in contradiction with numerical dynamo modeling results which show that non-reversing magnetic field behavior is more preferable when the CMB heat flux is low (Olson et al., 2010; Olson and Amit, 2014). Global mantle convection models with imposed surface plate motion history predicted an increase in global CMB heat flux during the mid-Cretaceous, which is difficult to explain the occurrence of the CNS (Zhang and Zhong, 2011).

Seismic observations have revealed two LLSVPs in the lowermost mantle, and the LLSVPs have been hypothesized to be caused by intrinsically dense and compositionally-distinct material. Recently, there have been efforts on understanding how the morphology of the LLSVPs links to the variation of CMB heat flux and formation of mantle plumes (Amit and Olson, 2015; Olson and Amit, 2015). One hypothesis as proposed by Olson and Amit (2015) is that the compositionally-distinct and intrinsically dense LLSVPs can be temporally elevated by the formation of mantle plumes. Whereas the later collapse of the LLSVPs on the CMB reduces the CMB heat flux and induces superchrons, the rise of mantle plumes to beneath the surface causes LIPs.

Numerical dynamo models suggest that, in addition to the global average of CMB heat flux, the spatial variation of CMB heat flux also affects the magnetic reversal frequency. In particular, the reversal frequency is more sensitive to changes of CMB heat flux at equatorial regions than other regions (Pétrélis et al., 2011; Heimpel and Evans, 2013). Our 2D models do not provide information about CMB heat flux at specific locations for the true Earth. In addition, we do not aim to study the spatial distribution of mantle plumes and LIPs with 2D models, which have been explored before (e.g., Li and Zhong, 2017). Our main goal here is to understand the basic physics process for the interaction between plumes and thermochemical piles and its effects on the CMB heat flux. We find that the basic physical process for the interaction between plumes and piles is generally consistent with the conceptual model by (Olson and Amit, 2015), although the relationship between plume pulses and CMB heat flux is different in most cases, as discussed below.

In some of our models, we find nearly periodic changes of the pile morphology and CMB heat flux. The periodic variations of CMB heat flux in some of our models is suggestive of the repetitive occurrence of geomagnetic superchrons during the Phanerozoic. The time interval between superchrons is ~150–200 Myr. To make a comparison with this information, we must convert the non-dimensional time used in our models to geological time. However, it needs to be pointed out that the geological time is not independently constrained by our non-dimensionalized models. The dimensional diffusion time varies significantly with the effective Rayleigh number of the mantle, and would be significantly over-estimated if the mantle viscosity used in a geodynamic model is higher than the viscosity of the true Earth which is not well constrained. A better approach is to scale model processes in terms of transit time (Zhong and Gurnis, 1993; Christensen and Hofmann, 1994):

$$t_G = \int_0^t \overline{u}(t')dt' \times t_{transit} \tag{10}$$

where t is the non-dimensional time, $\overline{u}(t')$ is the average absolute velocity on the surface at non-dimensional time t', and t_G is the geological time. Thus, the geological time is scaled by, and is very sensitive to, the magnitude of surface velocity. By definition, one transit time equals to the time takes for slabs to sink from the surface to the CMB, and in this study, we make the assumption that one mantle transit time equals to $t_{transit}$ = 60 Myr, following previous studies (Christensen and Hofmann, 1994; Li and McNamara, 2013). The dimensional-time scaled with the

transit time is plotted on the top axes in Fig. 4 for each panel. As shown in Fig. 4, the CMB heat flux changes with a typical period of ~100 Myr for cases 1, 2 and 3, and ~220 Myr for cases 7 and 8. These values are comparable with the observed time interval between Phanerozoic superchrons of ~150–200 Myr.

We find that it takes more time for the pile to grow than to collapse, and more time is required for the CMB heat flux to increase than to decrease (e.g., Fig. 4a and b). This asymmetry may explain why it takes a long time for the reversal rate to recover from a superchron, whereas superchron onset is more sudden (Olson and Amit, 2015). The CMB heat flux changes about 10–15% during each cycle for our reference case (e.g., Fig. 4a). This number sometimes increases up to ~50% when less viscous ppv phase is included in the cold regimes of the lowermost mantle (Fig. 4h). Numerical dynamo models suggest that superchron may occur by a small reduction of CMB heat flux (e.g., ~20% or smaller) when the geomagnetic field is close to the transition for the dynamo from hyperactivity to low activity (Driscoll and Olson, 2009; Olson et al., 2010). Thus, the reduction of CMB heat flux caused by the collapse of thermochemical piles in our models could be sufficient to induce superchrons.

Our results show good correlation between the evolution of morphology of thermochemical piles and global CMB heat flux. The large and periodic variation of CMB heat flux as inferred from the repetitive occurrence of superchrons during the Phanerozoic suggests that the two seismically observed LLSVPs in the lowermost mantle, if they are caused by thermochemical piles, may have switched coherently between phases of growth and collapse several times during this time, that are caused by the formation and rise of mantle plumes as suggested in our models. However, we show that when there are several mantle plumes with each plume interacting with only part of a large thermochemical pile, these plumes need to form in unison in order to have the largest effects on changing the height and the footprint of the LLSVPs and the CMB heat flux.

During the Cretaceous, the major phase of the LIP activity started slightly before and continued during the CNS, just when the CMB heat flux is supposed to be minimum (Olson and Amit, 2015). In contrast, the pulses of plume heat flux in our models typically occur near the peaks of CMB heat flux, in most cases well before the next CMB heat flux minimum (e.g., Fig. 4aand b). This happens for two main reasons. Firstly, the thermochemical piles start to collapse (and the CMB heat flux starts to decrease) typically after the thermal plumes detach from the top of the piles. If the top of the piles is high, the plumes need only to rise a relatively short distance before reaching the near-surface. Secondly, the hot and buoyant plume materials tend to rise through pre-existing plume conduits in our models (e.g., Figs. 3, 5, 6). Since the plume conduits have higher temperature and lower viscosity than the background mantle, plumes ascend much faster through pre-existing plume conduits than through the colder and more viscous background mantle. Accordingly, it takes little time for conduit plumes in our models to rises from the top of the pile to near the surface, so naturally the pulses of plume heat flux typically occur around the time when the piles start to collapse and the CMB heat flux is near maximum. However, as the pile shape becomes more complex, we find that it takes more time for the plumes to rise, particularly if the plumes bifurcate as illustrated in Fig. 7 or form on the pile margins and ascend through the viscous background mantle as illustrated in Fig. 8. In these situations, we find the pulses of plume heat flux occur later than the maxima in CMB heat flux (e.g., Fig. 4c and d), although in nearly every case, prior to the CMB heat flux minima. Therefore, in order for the pulses of plume flux to coincide with CMB heat flux minima (which would reconcile the LIP and geomagnetic observations) the rise time of LIP-forming mantle plumes would have to be even longer than in our models, or the LLSVPs collapse faster than the thermochemical piles in our models.

4.3. The role of slab subduction

Another possible influence on the links between the variations of CMB heat flux and plume heat flux that our models may fail to properly capture involves time variations in the subduction of cold slabs. The impinging of slabs on the CMB may horizontally push the pile edges to elevate the pile or to impede the collapse of the pile. The spreading of slabs on the CMB affects the lateral mantle flow velocity in the basal thermal boundary layer, which influences the location where mantle

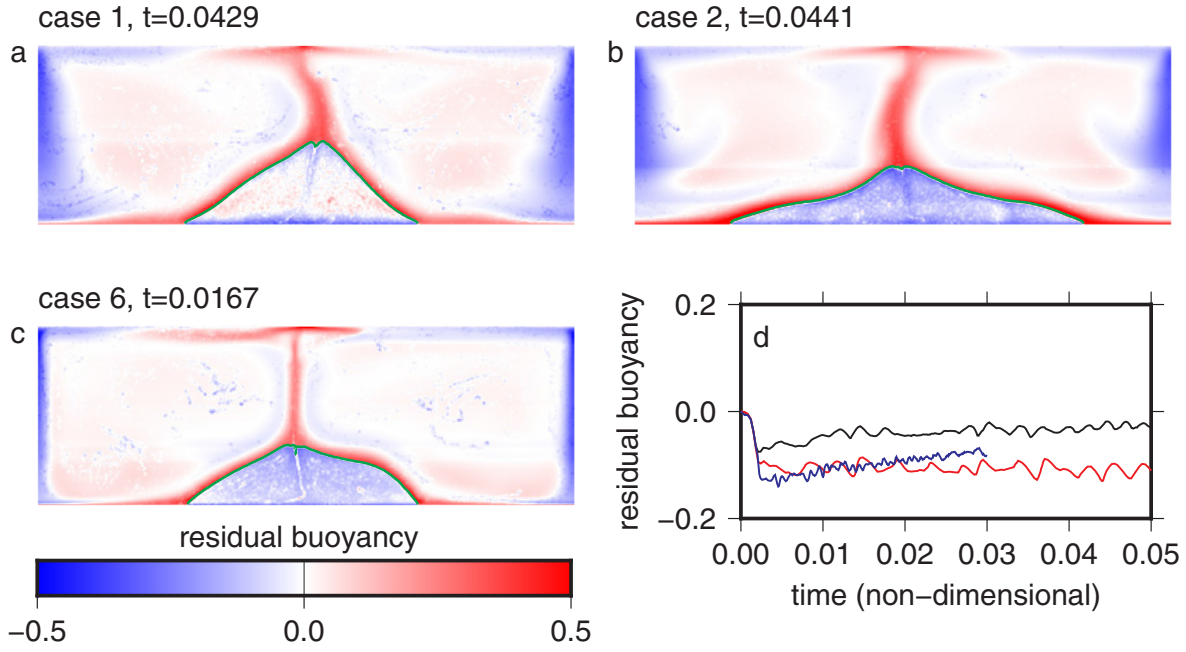

Fig. 14. a-c, residual buoyancy field for case 1 at t = 0.0429 (a), case 2 at t = 0.0441 (b), and case 6 at t = 0.0167 (c). d, time evolution of averaged residual buoyancy within the thermochemical pile for cases 1 (black line), 2 (red line) and 6 (blue line). (For interpretation of the references to colour in this figure legend, the reader is referred to the web version of this article.)

plumes form (Li and Zhong, 2017). Furthermore, the CMB heat flux is highest beneath regions with active subduction and the global mean CMB heat flux is largely controlled by the subduction process (Zhang and Zhong, 2011). If the pulses of subduction and plume formation are in phase, the variations of CMB heat flux and plume heat flux would be nearly in phase. However, if the two pulsations get out of phase for any reason, the links between the variations of CMB heat flux and plume heat flux may break. In our simplified 2D models, there is limited room for plumes and slabs to slip out of phase. In the Earth's mantle, the volume of cold slabs impinging the CMB and the temperature of their slabs are controlled by many factors, such as the surface processes, the effects of mantle transition zone and the viscosity structure of the mantle, but the formation of mantle plumes, which is the result of thermal boundary layer instability, is more controlled by the properties of the mantle near the CMB. Thus, the pulses of subduction to the lowermost mantle and the pulses of plume formation are possible to get out of phase in more complex models, particularly in the 3D mantle.

4.4. On the density and stability of thermochemical piles and LLSVPs

Our results show that the residual buoyancy (or the density anomaly) is not homogeneous within a thermochemical pile, similar to that found by Lassak et al. (2007) and Tan and Gurnis (2005). In particular, the major part of the pile in case 1 is nearly neutrally buoyant or slightly positively buoyant, and the pile is strongly negatively buoyant at the bottom and near the top of the pile (Figs. 3, 5, 14a). However, the residual buoyancy of a thermochemical pile strongly depends on factors such as the buoyancy number (or the intrinsic density) of the pile material and the density and volume of cold downwelling material surrounding the pile. For example, by increasing the buoyancy number to $B = 0.8$ in case 2, the thermochemical pile becomes largely negatively buoyant (Fig. 14b). In case 6, the volume of the cold downwellings decreases relative to case 1 and the residual buoyancy of the thermochemical pile is also largely negatively (Fig. 14c).

Fig. 14d shows the time evolution of the averaged residual buoyancy within the thermochemical pile for cases 1, 2 and 6. The pile has negative buoyancy respected to the background mantle in all three cases. The residual buoyancy of the pile is more negative in case 2 than case 1, which results in slower entrainment of pile material into the background mantle. However, although the pile is more negatively buoyant with respect to the surrounding mantle in case 6, it is less stable than in case 1. This is because the weak ppv phase in case 6 increases the entrainment rate of pile material into the background mantle.

The relative density of the LLSVPs with respect to the surrounding mantle, which has implications for the geoid (Liu and Zhong, 2016) as well as mantle convection, has proven difficult to constrain seismologically and remains a matter of debate (Ishii and Tromp, 1999; Resovsky and Ritzwoller, 1999; Koelemeijer et al., 2017; Lau et al., 2017). Our results indicate that, assuming the LLSVPs represent thermochemical piles, the density anomalies within the LLSVPs are not uniform, but instead vary from place to place, possibly negative in some regions and positive in others. Furthermore, the density of the LLSVPs is not the only factor that controls their stability. If one part of the LLSVPs is slightly less dense than the surrounding mantle, it does not necessarily indicate that the LLSVP structures themselves are unstable, because other parts of the same structure could have compensating excess density. Alternatively, the existence of ppv phase in the lowermost mantle tends to lower the viscosity adjacent to the LLSVPs, which may promote their instability, even if they are overall denser than the surrounding mantle.

5. Conclusion

Our calculations show that the formation of mantle plumes, the variation of CMB heat flux, and the morphologic changes to the thermochemical piles of large-scale compositional heterogeneity in the lowermost mantle are likely to be dynamically coupled. We find good correlation between the time variation of CMB heat flux and the changes of pile morphology. The interaction between mantle plumes and the thermochemical piles sometimes leads to periodic changes of CMB heat flux and regular pulses of plume heat flux.

We find that the morphology of a thermochemical pile fluctuates during the formation and ascent of mantle plumes. Piles can be significantly elevated by the initiation of strong mantle plumes, but after the plumes rise towards the surface and begin to stagnate at shallow depths, the piles start to collapse. While the arrival of plumes beneath the surface is expected to initiate enhanced surface volcanism, the collapse of the pile decreases the CMB heat flux. The timing between the variation of CMB heat flux and pulses of plume heat flux is largely controlled by how fast the plumes rise from the top of piles to near the surface, which in turn depends on whether the plumes access pre-existing conduits.

Repeated geomagnetic superchrons during the Phanerozoic may be the result of a quasi-periodic CMB heat flux variations, induced by the quasi-periodic formation of strong mantle plumes and quasi-periodic morphologic changes to the LLSVPs. The morphologic changes of the thermochemical piles induced by the formation of plumes cause up to ~20% CMB heat flux variations (higher in some models with weak ppv phase). The estimated periodicities of CMB heat flux variations in our models are ~100–200 Myr, in fundamental agreement with the spacing of Phanerozoic superchrons. One remaining problem is the time lag of the plume heat flux variations relative to the CMB heat flux variations, which is probably too short in our models.

Lastly, we find that the density anomaly within the thermochemical piles is heterogeneous, varying from place to place, although the average density anomaly for each pile is slightly higher than the surrounding mantle. This suggests that mantle LLSVPs also have heterogeneous distributions of density anomaly with respect to their surroundings, with the LLSVPs being slightly denser than the background mantle.

Acknowledgements

We would like to acknowledge high performance computing support from Yellowstone (ark:/85065/d7wd3xhc) provided by NCAR's Computational and Information Systems Laboratory, sponsored by the National Science Foundation. We thank Takashi Nakagawa and two anonymous reviewers for their constructive comments. This work is supported by National Science Foundation through Grants 1135382 and 1645245.

Appendix A. Supplementary data

Supplementary data associated with this article can be found, in the online version, at http://dx.doi.org/10.1016/j.pepi.2018.01.010.

References

Amit, H., Olson, P., 2015. Lower mantle superplume growth excites geomagnetic reversals. Earth Planet. Sci. Lett. 414, 68–76. http://dx.doi.org/10.1016/j.epsl.2015.01.013.

Ammann, M.W., Brodholt, J.P., Wookey, J., Dobson, D.P., 2010. First-principles constraints on diffusion in lower-mantle minerals and a weak D" layer. Nature 465, 462–465. http://dx.doi.org/10.1038/nature09052.

Biggin, A.J., Steinberger, B., Aubert, J., Suttie, N., Holme, R., Torsvik, T.H., van der Meer, D.G., van Hinsbergen, D.J.J., 2012. Possible links between long-term geomagnetic variations and whole-mantle convection processes. Nat. Geosci. 5, 526–533. http://dx.doi.org/10.1038/NGEO1521.

Bower, D.J., Gurnis, M., Seton, M., 2013. Lower mantle structure from paleogeographically constrained dynamic Earth models. Geochem. Geophys. Geosyst. 14, 44–63. http://dx.doi.org/10.1029/2012gc004267.

Campbell, I.H., 2005. Large igneous provinces and the mantle plume hypothesis. Elements 1, 265–269. http://dx.doi.org/10.2113/gselements.1.5.265.

Campbell, I.H., Griffiths, R.W., 1992. The changing nature of mantle hotspots through

time – implications for the chemical evolution of the Mantle. J. Geol. 100, 497–523.
Cande, S.C., Kent, D.V., 1995. Revised calibration of the geomagnetic polarity timescale for the Late Cretaceous and Cenozoic. J. Geophys. Res. 100, 6093–6095. http://dx.doi.org/10.1029/94JB03098.
Christensen, U.R., Hofmann, A.W., 1994. Segregation of subducted oceanic crust in the convecting mantle. J. Geophys. Res. 99, 19867–19884. http://dx.doi.org/10.1029/93JB03403.
Christensen, U.R., Yuen, D.A., 1985. Layered Convection Induced by Phase-Transitions. J. Geophys. Res. 90, 10291–10300. http://dx.doi.org/10.1029/Jb090ib12p10291.
Condie, K.C., Arndt, N., Davaille, A., Puetz, S.J., 2017. Zircon age peaks: production or preservation of continental crust? Geosphere. http://dx.doi.org/10.1130/ges01361.1.
Condie, K.C., Davaille, A., Aster, R.C., Arndt, N., 2014. Upstairs-downstairs: supercontinents and large igneous provinces, are they related? Int. Geol. Rev. 57, 1341–1348. http://dx.doi.org/10.1080/00206814.2014.963170.
Cottaar, S., Lekic, V., 2016. Morphology of seismically slow lower-mantle structures. Geophys. J. Int. 207, 1122–1136. http://dx.doi.org/10.1093/gji/ggw324.
Courtillot, V., Jaupart, C., Manighetti, I., Tapponnier, P., Besse, J., 1999. On causal links between flood basalts and continental breakup. Earth Planet. Sci. Lett. 166, 177–195. http://dx.doi.org/10.1016/S0012-821x(98)00282-9.
Courtillot, V., Olson, P., 2007. Mantle plumes link magnetic superchrons to phanerozoic mass depletion events. Earth Planet. Sci. Lett. 260, 495–504. http://dx.doi.org/10.1016/j.epsl.2007.06.003.
Courtillot, V.E., Renne, P.R., 2003. On the ages of flood basalt events. C.R. Geosci. 335, 113–140. http://dx.doi.org/10.1016/S1631-0713(03)00006-3.
Davaille, A., 1999. Two-layer thermal convection in miscible viscous fluids. J. Fluid Mech. 379, 223–253. http://dx.doi.org/10.1017/S0022112098003322.
Davies, G.F., 1988. Ocean bathymetry and mantle convection: 1. Large-scale flow and hotspots. J. Geophys. Res. 93, 10467–10480. http://dx.doi.org/10.1029/JB093iB09p10467.
Deschamps, F., Tackley, P.J., 2008. Searching for models of thermo-chemical convection that explain probabilistic tomography. Phys. Earth Planet. Int. 171, 357–373. http://dx.doi.org/10.1016/j.pepi.2008.04.016.
Deschamps, F., Tackley, P.J., 2009. Searching for models of thermo-chemical convection that explain probabilistic tomography. II–influence of physical and compositional parameters. Phys. Earth Planet. Int. 176, 1–18. http://dx.doi.org/10.1016/j.pepi.2009.03.012.
Driscoll, P., Olson, P., 2009. Effects of buoyancy and rotation on the polarity reversal frequency of gravitationally driven numerical dynamos. Geophys. J. Int. 178, 1337–1350. http://dx.doi.org/10.1111/j.1365-246X.2009.04234.x.
Dziewonski, A.M., Lekic, V., Romanowicz, B.A., 2010. Mantle anchor structure: an argument for bottom up tectonics. Earth Planet. Sci. Lett. 299, 69–79. http://dx.doi.org/10.1016/j.epsl.2010.08.013.
Ernst, R., Bleeker, W., 2010. Large igneous provinces (LIPs), giant dyke swarms, and mantle plumes: significance for breakup events within Canada and adjacent regions from 2.5 Ga to the Present. Can. J. Earth Sci. 47, 695–739. http://dx.doi.org/10.1139/E10-025.
French, S.W., Romanowicz, B., 2015. Broad plumes rooted at the base of the Earth's mantle beneath major hotspots. Nature 525, 95–99. http://dx.doi.org/10.1038/nature14876.
Garnero, E.J., McNamara, A.K., Shim, S.-H., 2016. Continent-sized anomalous zones with low seismic velocity at the base of Earth's mantle. Nat. Geosci. 9, 481–489. http://dx.doi.org/10.1038/ngeo2733.
Grand, S.P., 2002. Mantle shear-wave tomography and the fate of subducted slabs. Philos. Trans. R. Soc. London Ser. A 360, 2475–2491. http://dx.doi.org/10.1098/rsta.2002.1077.
Gu, Y.J., Dziewonski, A.M., Su, W., Ekström, G., 2001. Models of the mantle shear velocity and discontinuities in the pattern of lateral heterogeneities. J. Geophys. Res. 106, 11169–11199. http://dx.doi.org/10.1029/2001jb000340.
Hager, B.H., 1984. Subducted slabs and the geoid: constraints on mantle rheology and flow. J. Geophys. Res. 89, 6003–6015. http://dx.doi.org/10.1029/JB089iB07p06003.
Haggerty, S.E., 1994. Superkimberlites: A geodynamic diamond window to the Earth's core. Earth Planet. Sci. Lett. 122, 57–69. http://dx.doi.org/10.1016/0012-821x(94)90051-5.
He, Y., Wen, L., 2012. Geographic boundary of the "Pacific Anomaly" and its geometry and transitional structure in the north. J. Geophys. Res. 117, B09308. http://dx.doi.org/10.1029/2012jb009436.
Heimpel, M.H., Evans, M.E., 2013. Testing the geomagnetic dipole and reversing dynamo models over Earth's cooling history. Phys. Earth Planet. Int. 224, 124–131. http://dx.doi.org/10.1016/j.pepi.2013.07.007.
Hunt, S.A., Weidner, D.J., Li, L., Wang, L.P., Walte, N.P., Brodholt, J.P., Dobson, D.P., 2009. Weakening of calcium iridate during its transformation from perovskite to post-perovskite. Nat. Geosci. 2, 794–797. http://dx.doi.org/10.1038/Ngeo663.
Ishii, M., Tromp, J., 1999. Normal-mode and free-air gravity constraints on lateral variations in velocity and density of Earth's mantle. Science 285, 1231–1236. http://dx.doi.org/10.1126/science.285.5431.1231.
Karato, S., 2010. The influence of anisotropic diffusion on the high-temperature creep of a polycrystalline aggregate. Phys. Earth Planet. Int. 183, 468–472. http://dx.doi.org/10.1016/j.pepi.2010.09.001.
King, S.D., Gable, C.W., Weinstein, S.A., 1992. Models of convection-driven tectonic plates: a comparison of methods and results. Geophys. J. Int. 109, 481–487. http://dx.doi.org/10.1111/j.1365-246X.1992.tb00111.x.
Koelemeijer, P., Deuss, A., Ritsema, J., 2017. Density structure of Earth's lowermost mantle from Stoneley mode splitting observations. Nat. Commun. 8, 15241. http://dx.doi.org/10.1038/ncomms15241.
Larson, R.L., 1991. Latest pulse of Earth: evidence for a mid-Cretaceous superplume. Geology 19, 547–550. http://dx.doi.org/10.1130/0091-7613(1991)019<0547:lpoeef>2.3.co;2.
Larson, R.L., Kincaid, C., 1996. Onset of mid-Cretaceous volcanism by elevation of the 670 km thermal boundary layer. Geology 24, 551–554. http://dx.doi.org/10.1130/0091-7613(1996)024<0551:OOMCVB>2.3.CO;2.
Larson, R.L., Olson, P., 1991. Mantle plumes control magnetic reversal frequency. Earth Planet. Sci. Lett. 107, 437–447. http://dx.doi.org/10.1016/0012-821X(91)90091-U.
Lassak, T.M., McNamara, A.K., Zhong, S., 2007. Influence of thermochemical piles on topography at Earth's core-mantle boundary. Earth Planet. Sci. Lett. 261, 443–455. http://dx.doi.org/10.1016/j.epsl.2007.07.015.
Lau, H.C.P., Mitrovica, J.X., Davis, J.L., Tromp, J., Yang, H.-Y., Al-Attar, D., 2017. Tidal tomography constrains Earth's deep-mantle buoyancy. Nature 551, 321. http://dx.doi.org/10.1038/nature24452.
Le Bars, M., Davaille, A., 2004. Large interface deformation in two-layer thermal convection of miscible viscous fluids. J. Fluid Mech. 499, 75–110. http://dx.doi.org/10.1017/S0022112003006931.
Leng, W., Zhong, S.J., 2008. Controls on plume heat flux and plume excess temperature. J. Geophys. Res. 113, B04408. http://dx.doi.org/10.1029/2007jb005155.
Li, M., McNamara, A.K., 2013. The difficulty for subducted oceanic crust to accumulate at the Earth's core-mantle boundary. J. Geophys. Res. 118, 1807–1816. http://dx.doi.org/10.1002/Jgrb.50156.
Li, M., McNamara, A.K., Garnero, E.J., 2014a. Chemical complexity of hotspots caused by cycling oceanic crust through mantle reservoirs. Nat. Geosci. 7, 366–370. http://dx.doi.org/10.1038/Ngeo2120.
Li, M., Zhong, S., 2017. The source location of mantle plumes from 3D spherical models of mantle convection. Earth Planet. Sci. Lett. 478, 47–57. http://dx.doi.org/10.1016/j.epsl.2017.08.033.
Li, X.D., Romanowicz, B., 1996. Global mantle shear velocity model developed using nonlinear asymptotic coupling theory. J. Geophys. Res. 101, 22245–22272. http://dx.doi.org/10.1029/96JB01306.
Li, Y., Deschamps, F., Tackley, P.J., 2014b. Effects of low-viscosity post-perovskite on the stability and structure of primordial reservoirs in the lower mantle. Geophys. Res. Lett. 41, 7089–7097. http://dx.doi.org/10.1002/2014GL061362.
Lin, S.C., van Keken, P.E., 2005. Multiple volcanic episodes of flood basalts caused by thermochemical mantle plumes. Nature 436, 250–252. http://dx.doi.org/10.1038/Nature03697.
Liu, X., Zhong, S.J., 2016. Constraining mantle viscosity structure for a thermochemical mantle using the geoid observation. Geochem. Geophys. Geosyst. 17, 895–913. http://dx.doi.org/10.1002/2015gc006161.
Masters, G., Laske, G., Bolton, H., Dziewonski, A., 2000. The relative behavior of shear veocity, bulk sound speed, and compressional velocity in the mantle: implications for chemical and thermal structure. In: al., S.K.E. (Ed.), Earth's Deep Interior: Mineral Physics and Tomography From the Atomic to the Global Scale. AGU Geophysical Monograph, Washington, D.C., pp. 63–86.
McNamara, A.K., Zhong, S., 2005. Thermochemical structures beneath Africa and the Pacific Ocean. Nature 437, 1136–1139. http://dx.doi.org/10.1038/nature04066.
Moresi, L.N., Solomatov, V.S., 1995. Numerical investigation of 2d convection with extremely large viscosity variations. Phys. Fluids 7, 2154–2162. http://dx.doi.org/10.1063/1.868465.
Murakami, M., Hirose, K., Kawamura, K., Sata, N., Ohishi, Y., 2004. Post-perovskite phase transition in MgSiO3. Science 304, 855–858. http://dx.doi.org/10.1126/science.1095932.
Nakagawa, T., Tackley, P.J., 2004. Effects of a perovskite-post perovskite phase change near core-mantle boundary in compressible mantle convection. Geophys. Res. Lett. 31, L16611. http://dx.doi.org/10.1029/2004gl020648.
Nakagawa, T., Tackley, P.J., 2005. The interaction between the post-perovskite phase change and a thermo-chemical boundary layer near the core-mantle boundary. Earth Planet. Sci. Lett. 238, 204–216. http://dx.doi.org/10.1016/j.epsl.2005.06.048.
Nakagawa, T., Tackley, P.J., 2011. Effects of low-viscosity post-perovskite on thermo-chemical mantle convection in a 3-D spherical shell. Geophys. Res. Lett. 38, L04309. http://dx.doi.org/10.1029/2010gl046494.
Ni, S., Helmberger, D.V., 2003. Ridge-like lower mantle structure beneath South Africa. J. Geophys. Res. 108, 2094. http://dx.doi.org/10.1029/2001jb001545.
Ni, S., Tan, E., Gurnis, M., Helmberger, D., 2002. Sharp sides to the African Superplume. Science 296, 1850–1852. http://dx.doi.org/10.1126/science.1070698.
O'Farrell, K.A., Lowman, J.P., 2010. Emulating the thermal structure of spherical shell convection in plane-layer geometry mantle convection models. Phys. Earth Planet. Int. 182, 73–84. http://dx.doi.org/10.1016/j.pepi.2010.06.010.
Olson, P., Amit, H., 2014. Magnetic reversal frequency scaling in dynamos with thermochemical convection. Phys. Earth Planet. Int. 229, 122–133. http://dx.doi.org/10.1016/j.pepi.2014.01.009.
Olson, P., Amit, H., 2015. Mantle superplumes induce geomagnetic superchrons. Front. Earth Sci. 3. http://dx.doi.org/10.3389/feart.2015.00038.
Olson, P., Hinnov, L.A., Driscoll, P.E., 2014. Nonrandom geomagnetic reversal times and geodynamo evolution. Earth Planet. Sci. Lett. 388, 9–17. http://dx.doi.org/10.1016/j.epsl.2013.11.038.
Olson, P., Nam, I.S., 1986. Formation of seafloor swells by mantle plumes. J. Geophys. Res. 91, 7181–7191. http://dx.doi.org/10.1029/JB091iB07p07181.
Olson, P.L., Coe, R.S., Driscoll, P.E., Glatzmaier, G.A., Roberts, P.H., 2010. Geodynamo reversal frequency and heterogeneous core-mantle boundary heat flow. Phys. Earth Planet. Int. 180, 66–79. http://dx.doi.org/10.1016/j.pepi.2010.02.010.
Pétrélis, F., Besse, J., Valet, J.P., 2011. Plate tectonics may control geomagnetic reversal frequency. Geophys. Res. Lett. 38. http://dx.doi.org/10.1029/2011GL048784.
Resovsky, J.S., Ritzwoller, M.H., 1999. Regularization uncertainty in density models estimated from normal mode data. Geophys. Res. Lett. 26, 2319–2322. http://dx.doi.

org/10.1029/1999GL900540.
Richards, M.A., Duncan, R.A., Courtillot, V.E., 1989. Flood basalts and hot-spot tracks: plume heads and tails. Science 246, 103–107. http://dx.doi.org/10.1126/science.246.4926.103.
Ritsema, J., Deuss, A., van Heijst, H.J., Woodhouse, J.H., 2011. S40RTS: a degree-40 shear-velocity model for the mantle from new Rayleigh wave dispersion, teleseismic traveltime and normal-mode splitting function measurements. Geophys. J. Int. 184, 1223–1236. http://dx.doi.org/10.1111/j.1365-246X.2010.04884.x.
Su, W., Mutter, C.Z., Mutter, J.C., Buck, W.R., 1994. Some theoretical predictions on the relationships among spreading rate, mantle temperature, and crustal thickness. J. Geophys. Res. 99, 3215–3227. http://dx.doi.org/10.1029/93JB02965.
Tan, E., Gurnis, M., 2005. Metastable superplumes and mantle compressibility. Geophys. Res. Lett. 32, L20307. http://dx.doi.org/10.1029/2005GL024190.
Tan, E., Leng, W., Zhong, S.J., Gurnis, M., 2011. On the location of plumes and lateral movement of thermochemical structures with high bulk modulus in the 3-D compressible mantle. Geochem. Geophys. Geosyst. 12, Q07005. http://dx.doi.org/10.1029/2011gc003665.
Trampert, J., Deschamps, F., Resovsky, J., Yuen, D., 2004. Probabilistic tomography maps chemical heterogeneities throughout the lower mantle. Science 306, 853–856. http://dx.doi.org/10.1126/science.1101996.
Wen, L., Silver, P., James, D., Kuehnel, R., 2001. Seismic evidence for a thermo-chemical boundary at the base of the Earth's mantle. Earth Planet. Sci. Lett. 189, 141–153. http://dx.doi.org/10.1016/S0012-821X(01)00365-X.
Whitehead, J.A., Luther, D.S., 1975. Dynamics of laboratory diapir and plume models. J. Geophys. Res. 80, 705–717. http://dx.doi.org/10.1029/JB080i005p00705.
Zhang, N., Zhong, S., Leng, W., Li, Z.-X., 2010. A model for the evolution of the Earth's mantle structure since the Early Paleozoic. J. Geophys. Res. 115, B06401. http://dx.doi.org/10.1029/2009jb006896.
Zhang, N., Zhong, S.J., 2011. Heat fluxes at the Earth's surface and core-mantle boundary since Pangea formation and their implications for the geomagnetic superchrons. Earth Planet. Sci. Lett. 306, 205–216. http://dx.doi.org/10.1016/j.epsl.2011.04.001.
Zhong, S., 2006. Constraints on thermochemical convection of the mantle from plume heat flux, plume excess temperature, and upper mantle temperature. J. Geophys. Res. 111, B04409. http://dx.doi.org/10.1029/2005jb003972.
Zhong, S.J., Gurnis, M., 1993. Dynamic feedback between a continentlike raft and thermal convection. J. Geophys. Res. 98, 12219–12232. http://dx.doi.org/10.1029/93jb00193.
Zhong, S.J., Gurnis, M., 1994. Role of plates and temperature-dependent viscosity in phase-change dynamics. J. Geophys. Res. 99, 15903–15917. http://dx.doi.org/10.1029/94jb00545.
Zhong, S.J., Rudolph, M.L., 2015. On the temporal evolution of long-wavelength mantle structure of the Earth since the early Paleozoic. Geochem. Geophys. Geosyst. 16, 1599–1615. http://dx.doi.org/10.1002/2015gc005782.